ROCK1 and 2 differentially regulate actomyosin organization to drive cell and synaptic polarity

Karen A. Newell-Litwa,[1] Mathilde Badoual,[2] Hannelore Asmussen,[1] Heather Patel,[1] Leanna Whitmore,[1] and Alan Rick Horwitz[1]

[1]Department of Cell Biology, University of Virginia School of Medicine, Charlottesville, VA 22908
[2]Laboratoire Imagerie et Modélisation en Neurobiologie et Cancérologie (IMNC), UMR 8165, Centre National de la Recherche Scientifique, University Paris-Sud and University Paris Diderot, 91405 Orsay, France

RhoGTPases organize the actin cytoskeleton to generate diverse polarities, from front–back polarity in migrating cells to dendritic spine morphology in neurons. For example, RhoA through its effector kinase, RhoA kinase (ROCK), activates myosin II to form actomyosin filament bundles and large adhesions that locally inhibit and thereby polarize Rac1-driven actin polymerization to the protrusions of migratory fibroblasts and the head of dendritic spines. We have found that the two ROCK isoforms, ROCK1 and ROCK2, differentially regulate distinct molecular pathways downstream of RhoA, and their coordinated activities drive polarity in both cell migration and synapse formation. In particular, ROCK1 forms the stable actomyosin filament bundles that initiate front–back and dendritic spine polarity. In contrast, ROCK2 regulates contractile force and Rac1 activity at the leading edge of migratory cells and the spine head of neurons; it also specifically regulates cofilin-mediated actin remodeling that underlies the maturation of adhesions and the postsynaptic density of dendritic spines.

Introduction

Structural and functional polarity underlies cellular activities as diverse as cell migration (Vicente-Manzanares et al., 2009), epithelial barrier formation (Shin et al., 2006), and synaptic plasticity in learning and memory (Bosch and Hayashi, 2012). In each case, the coordinated activity of the small RhoGTPases, RhoA and Rac1, regulates the actin organization that supports this polarization (Nobes and Hall, 1999; Heasman and Ridley, 2008; Rex et al., 2009). In migrating cells, for example, RhoA activates nonmuscle myosin II, resulting in actomyosin filament bundles that define the sides and rear (Chrzanowska-Wodnicka and Burridge, 1996; Kolega, 2003; Vicente-Manzanares et al., 2008) and localizes Rac1 activity to the cell front (Vicente-Manzanares et al., 2011), where it nucleates and mediates actin polymerization to form protrusions (Ridley et al., 1992). Likewise, in synaptic development and plasticity, Rac1 drives formation of filopodia-like spine precursors, which subsequently mature through RhoA-dependent myosin II activation into polarized mushroom-shaped spines (Tashiro and Yuste, 2004; Hodges et al., 2011). Further excitatory stimulation associated with long-term potentiation (LTP) leads to Rac1-driven spine head expansion (Tashiro and Yuste, 2004; Rex et al., 2009).

In both migratory and neuronal cells, Rac1 and RhoA exhibit reciprocal as well as spatially or temporally segregated activities (Leeuwen et al., 1997; Hirose et al., 1998; Sander et al., 1999; Wong et al., 2000; Nimnual et al., 2003; Wildenberg et al., 2006; Sanz-Moreno et al., 2008; Machacek et al., 2009). Constitutive Rac1 activation inhibits RhoA, preventing the formation of RhoA-driven actomyosin filament bundles and mature adhesions. This is also seen by inhibition of myosin activity with either the myosin II inhibitor, blebbistatin, or RhoA kinase (ROCK) inhibitor, Y-27632 (Sander et al., 1999; Kuo et al., 2011). Conversely, RhoA activity and its associated actomyosin contractility inhibit Rac1 activity at the sides and rear of polarized migratory cells (Katsumi et al., 2002; Vicente-Manzanares et al., 2011). How RhoA antagonizes Rac1 activity is unclear, although mechanotransduction and/or the activity of a specific downstream effector, such as ROCK, are two attractive hypotheses (Katsumi et al., 2002).

ROCK is a major downstream RhoA effector and activates myosin II by phosphorylation of myosin regulatory light chain (RLC) on Thr18 and Ser19, directly and/or indirectly through inactivation of myosin light chain phosphatase (MLCP; Kimura et al., 1996; Amano et al., 1997; Totsukawa et al., 2000; Katoh et al., 2001). In migrating cells, diphosphorylation of both RLC Thr18 and Ser19 results in the formation of stable actomyo-

Correspondence to Karen A. Newell-Litwa: kal8m@virginia.edu

Abbreviations used in this paper: CMV, cytomegalovirus; DIV, days in vitro; FRET, fluorescence resonance energy transfer; LTP, long-term potentiation; MIIB, myosin IIB; MLCP, myosin light chain phosphatase; PAK, p21-activated kinase; PBD, protein binding domain; PSD, postsynaptic density; RLC, regulatory light chain; ROCK, RhoA kinase; ROI, region of interest; TIRF, total internal reflection; WT, wild type.

The Rockefeller University Press $30.00
J. Cell Biol. Vol. 210 No. 2 225–242
www.jcb.org/cgi/doi/10.1083/jcb.201504046

sin filament bundles and large elongated adhesions (Amano et al., 1997). Analogously, RLC diphosphorylation drives dendritic spine maturation into a polarized mushroom shape and increases the size of the postsynaptic density (PSD; Hodges et al., 2011). The ROCK inhibitor Y-27632 decreases RLC phosphorylation, resulting in the loss of actomyosin filament bundles and a concomitant up-regulation in Rac1 activity (Uehata et al., 1997; Tsuji et al., 2002; Kolega, 2003). It also disrupts adhesion maturation and produces extensive lamellipodia in migrating cells (Ishizaki et al., 2000; Tsuji et al., 2002; Worthylake and Burridge, 2003) and similarly disrupts maturation of dendritic spines into a polarized mushroom shape in neurons (Tashiro and Yuste, 2004; Hodges et al., 2011).

However, there are two ROCK isoforms, ROCK1 and ROCK2, and Y-27632 indiscriminately targets both (Ishizaki et al., 2000). The use of Y-27632 to target ROCK-mediated actomyosin contractility has thus obscured possible differences in isoform-specific functions, making it unclear whether myosin II activation and Rac1 inactivation are jointly or independently regulated downstream of RhoA. Although ROCK1 and ROCK2 exhibit 90% homology in their kinase domain and 64% homology overall (Leung et al., 1996; Julian and Olson, 2014), some evidence points to isoform-specific roles in polarity. For example, knockdown of ROCK1, but not ROCK2, altered actin filament bundle formation and adhesion maturation in fibroblasts (Yoneda et al., 2005), whereas ROCK2 specifically affected chemotaxis of prostate cancer cells (Vega et al., 2011). Whether these two isoforms differentially impact dendritic spine development is as yet unexplored.

In light of a role for ROCK-mediated myosin activity in Rac1/RhoA reciprocity and the presence of two poorly distinguished ROCK isoforms, we sought to define the roles of ROCK1 and 2 in myosin II regulation and Rac1 activity in both dendritic spine polarity in neurons and front–rear polarity in migratory fibroblasts. Using isoform-specific knockdowns, we demonstrate distinct, but conserved, roles for ROCK1 and ROCK2. In both systems, ROCK1 specifically mediates RLC T18 and S19 diphosphorylation, leading to stable actomyosin bundle formation and polarity. Although ROCK1 partitions Rac1 activity to the cell front, it does not regulate its activity. In contrast, ROCK2 monophosphorylates RLC S19 to generate contractile forces that correlate inversely with Rac1 activity. In addition to regulating polarity through myosin activity, ROCK2 phosphorylated the actin-severing protein cofilin on Ser3, resulting in adhesion and PSD maturation. Thus, polarity in both systems results from the coordinated, but distinct, activities of the two ROCK isoforms and underscores the need for isoform-specific pharmacological inhibitors of ROCK activity.

Results

ROCK1 and 2 localize to specific actin assemblies

To better understand whether ROCK1 and ROCK2 differentially regulate actin organization, we examined the localization of fluorescently labeled ROCK constructs. At low levels of expression, ROCK1 and ROCK2 exhibited specific subcellular localization patterns. GFP-ROCK1 strongly localized to actomyosin filament bundles along the cell sides and rear (Fig. 1 A, *f1* and *f2*). However, GFP-ROCK2 additionally localized to actin filaments within protrusions (Fig. 1 A, arrowheads, compare ROCK1 in protrusions *p1* and *p2* with ROCK2 in protrusions *p3* and *p4*). Ratiometric imaging of GFP-tagged ROCK constructs and phalloidin-stained actin confirmed this difference in isoform-specific localizations (Fig. 1 B). These observed subcellular localizations lead us to hypothesize that these ROCK isoforms may distinctly regulate actin organization underlying cell polarity. Specifically, we hypothesized that ROCK1 may regulate the formation of actomyosin filament bundles at the cell rear, whereas the additional localization of ROCK2 to protrusions uniquely positions it to regulate actin polymerization at the front of the cell.

ROCK1 and ROCK2 differentially phosphorylate the myosin RLC and actin-severing protein cofilin

To assess whether ROCK1/2 differentially regulate actomyosin organization underlying front–back polarity, we examined the phosphorylation of ROCK targets, including myosin RLC and the actin-severing protein cofilin. RhoA activates nonmuscle myosin II by ROCK-mediated phosphorylation of the myosin RLC on residues Thr18 and Ser19 (Amano et al., 1996). In both migrating cells and synapse formation, diphosphorylation of both Thr18 and Ser19 generates actomyosin filament bundles that define the cell rear and mature spine, respectively (Vicente-Manzanares and Horwitz, 2010; Hodges et al., 2011). These stable actomyosin filament bundles drive adhesion and PSD maturation (Vicente-Manzanares and Horwitz, 2010; Hodges et al., 2011). In contrast, monophosphorylation of Ser19 alone results in less stable actomyosin filament bundles, which regulate early stages of adhesion maturation within protrusions of migrating cells, and similarly produce dynamic filopodia-like spine precursors with small PSDs in neurons (Vicente-Manzanares and Horwitz, 2010; Hodges et al., 2011).

To determine which isoform, ROCK1 or ROCK2, mediates these specific RLC phosphorylations, we used isoform-specific shRNAs to down-regulate ROCK in CHO.K1 fibroblasts (Fig. 2, A–C), in which the roles of RLC phosphorylations are well characterized (Vicente-Manzanares et al., 2008; Vicente-Manzanares and Horwitz, 2010). We assessed the levels of phosphorylated RLC with two antibodies, one specific for RLC (S19P) and the other for diphosphorylated RLC (T18P, S19P). Although knockdown of either ROCK1 or ROCK2 decreased phosphorylation of MLCP (Fig. S5), ROCK2 significantly reduced the levels of monophosphorylated RLC S19 (Fig. 2, D and F), whereas only ROCK1 significantly reduced the levels of diphosphorylated RLC in either CHO.K1 (Fig. 2, E and F) or the more contractile REF-52 cell line (Fig. 2, I and J). Reduced RLC phosphorylation was observed even though cells were treated with the MLCP inhibitor, calyculin A, demonstrating that ROCK1 and 2 are not acting solely through inactivation of MLCP (Totsukawa et al., 2000).

In addition to the formation of actomyosin filament bundles, ROCK regulates Rac1-driven actin polymerization via cofilin S3 phosphorylation (Maekawa et al., 1999; Watanabe et al., 2007b). Cofilin both severs and depolymerizes actin filaments (DesMarais et al., 2005); however, phosphorylation of cofilin on Ser3 abolishes its actin association, preventing actin remodeling (DesMarais et al., 2005). Knockdown of ROCK2, but not ROCK1, specifically reduced cofilin S3 phosphorylation (Fig. 2, G and H). Thus, in addition to regulating myosin II activity through RLC S19 monophosphorylation, ROCK2 also regulates actin polymerization through cofilin S3 phosphorylation.

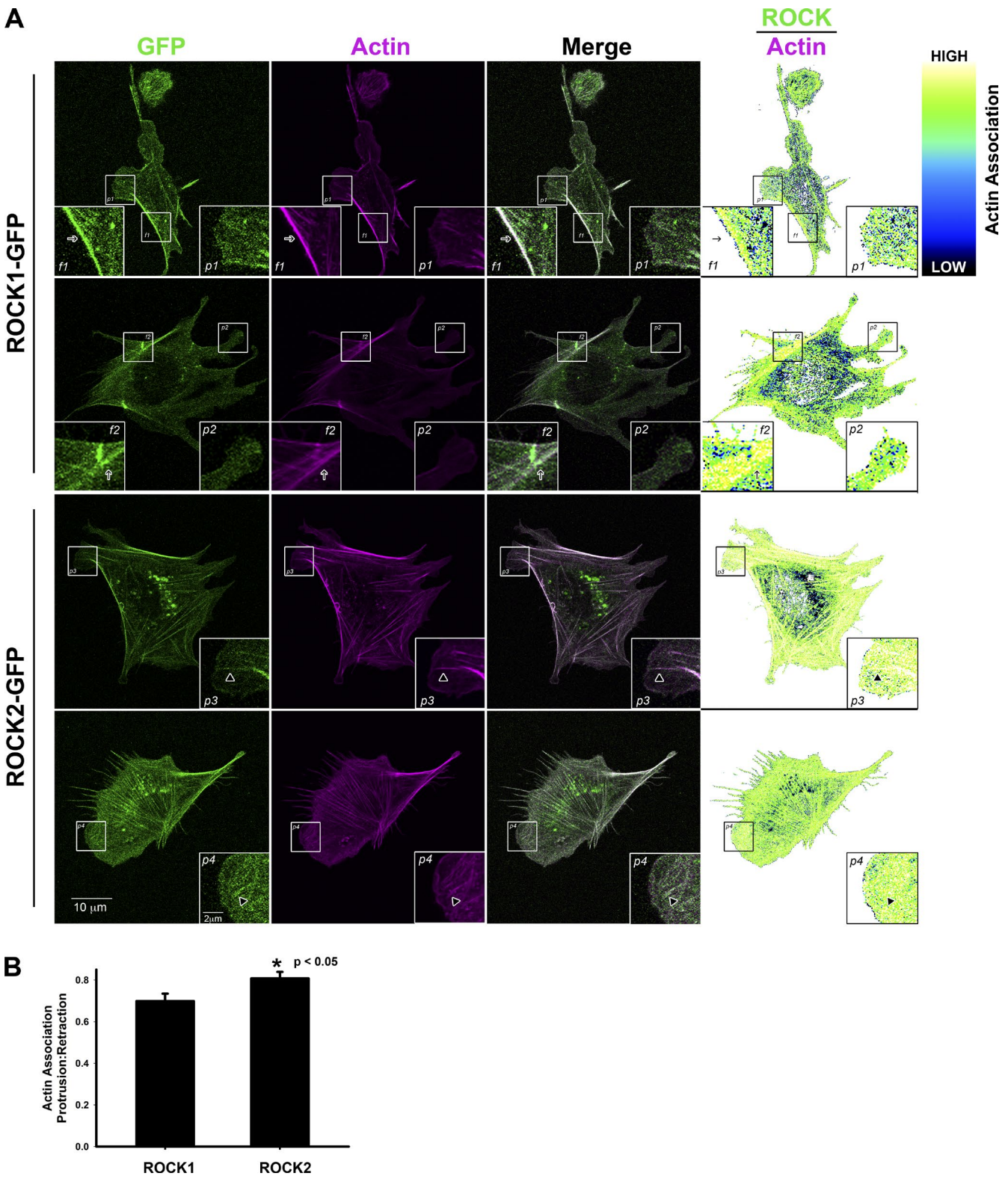

Figure 1. **ROCK1 preferentially localizes to actomyosin filament bundles, whereas ROCK2 also localizes to membrane protrusions.** (A) Representative CHO.K1 cells expressing either ROCK1-GFP (top two rows) or ROCK2-GFP (bottom two rows) and costained for rhodamine phalloidin. Ratiometric images on the right were created by dividing the ROCK-GFP signal by rhodamine phalloidin; intensity was inverted so that areas of greatest actin association are brighter. *f* indicates actomyosin filament bundles; *p* indicates protrusions. Arrows indicate actin filament bundles at the rear of the cell, and arrowheads indicate actin filaments within protrusions. (B) Quantification of the mean intensity of the ratiometric image in protrusions versus actomyosin filament bundles at the rear of the cell. ROCK2-GFP similarly localizes to both actin filaments in protrusions and actomyosin filament bundles, resulting in a ratio approaching 1. n = 14 ROCK1-GFP– and 14 ROCK2-GFP–expressing cells. Error bars indicate SEM.

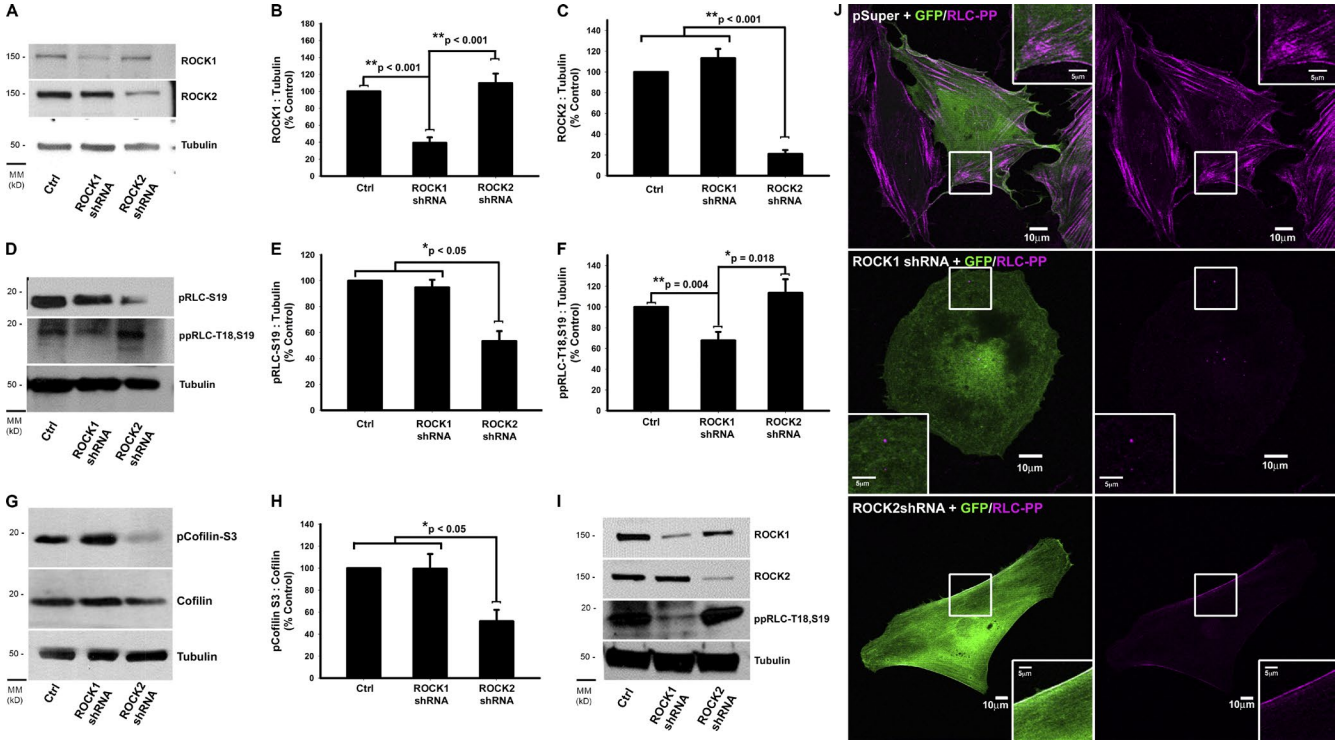

Figure 2. **ROCK1 and ROCK2 differentially phosphorylate the myosin RLC and actin-severing protein, cofilin.** CHO.K1 cells were harvested 48–72 h after transfection with ROCK isoform-specific shRNAs and were pretreated with 10 nM Calyculin A for 10 min. (A–C) Western blot of ROCK1, ROCK2, and tubulin, and the corresponding analysis of ROCK1 (B) and ROCK2 (C) protein levels normalized to tubulin. (D–F) Western blot of RLC S19 phosphorylation, RLC T18, S19 diphosphorylation, and tubulin and the corresponding analysis of RLC S19 phosphorylation (E) and RLC T18, S19 diphosphorylation (F) normalized to tubulin. (G and H) Western blot of cofilin S3 phosphorylation, total cofilin, and tubulin, and the corresponding analysis of the ratio of phosphorylated cofilin to total cofilin (H), normalized for tubulin expression. (I) Western blot of untreated REF-52 cells lysed 48 h after transfection with rat isoform-specific ROCK shRNAs and probed for ROCK1, ROCK2, diphosphorylated RLC T18P, S19P, and tubulin. (J) Immunofluorescence of REF-52 cells cotransfected with GFP and either control pSUPER empty vector or ROCK isoform–specific shRNAs were plated on 2 μg/ml fibronectin for 4 h and immunostained for diphosphorylated RLC T18P, S19P. Error bars indicate SEM. Ctrl, control; MM, molecular mass.

To assess how the differential phosphoregulation of RLC and cofilin by ROCK1 and 2 contributes to polarity, we used phosphomimetic mutants to rescue the observed knockdown phenotypes. We calculated the polarity index as the ratio of cell length to cell width, such that round, nonpolarized cells exhibit a polarity index of 1. Control cells begin to polarize within 2 h of plating on fibronectin and continue to polarize through the next several hours (Fig. 3, A and C). However, CHO.K1 cells with ROCK1 knocked down failed to polarize even when plated overnight on fibronectin, consistent with previous evidence that ROCK1 depletion produces a rounded morphology in primary rat embryonic fibroblasts plated for 24–72 h on fibronectin (Fig. 3, A and C; Yoneda et al., 2005). ROCK1-deficient REF-52 cells were similarly round and, in addition to decreased RLC diphosphorylation, also exhibited disorganized microtubules (Fig. S1). This is consistent with reports that nonmuscle myosin II contractility restricts and organizes microtubules in both neurons and fibroblasts (Fukushima and Morita, 2006; Even-Ram et al., 2007; Rösner et al., 2007; Burnette et al., 2008). Notably, expression of diphosphomimetic RLC-T18D, S19D rescued polarity in ROCK1-deficient cells (Fig. 3 D), demonstrating that ROCK1 establishes cell polarity through RLC T18, S19 diphosphorylation.

Opposite to the phenotype observed with ROCK1 knockdown, ROCK2 knockdown cells are more elongated and exhibit an increased perimeter when compared with either control or ROCK1 knockdown cells, even after overnight plating on fibronectin (Fig. 3, A–C). Knockdown of ROCK2 accelerated polarity, such that the ROCK2 knockdown cells exhibited a polarity index similar to control cells plated overnight after only 2 h of plating on fibronectin (Fig. 3 C). Unlike the elongated morphology previously observed when ROCK2 knockdown cells were plated on fibronectin for extended time periods (24–72 h; Yoneda et al., 2005), we consistently observed increased membrane protrusions in both CHO.K1 and REF52 cells spread for shorter time periods (2 h or overnight). However, expression of a cofilin-S3D phosphomimetic mutant or monophosphomimetic RLC-T18A, S19D reduced the polarity index of ROCK2 knockdown cells to levels similar to those observed in control cells (Fig. 3 E). Notably, diphosphomimetic RLC-T18D, S19D did not affect the axis ratio of ROCK2 knockdown cells nor did expression of cofilin S3D alter the polarity of ROCK1 knockdown cells (Fig. S2), further demonstrating that ROCK1 and ROCK2 regulate distinct signaling pathways in the formation of front–back migratory cell polarity.

ROCK1 initiates front–back polarity of migratory cells and the dendritic spine

Because ROCK inhibition alters actomyosin bundle organization, we assessed the effect of ROCK1-mediated RLC diphosphorylation on the organization of GFP-tagged nonmuscle myosin IIB (MIIB), which is preferentially regulated by RLC diphosphorylation and responsible for the formation of large, stable actomyosin bundles (Vicente-Manzanares et al., 2008,

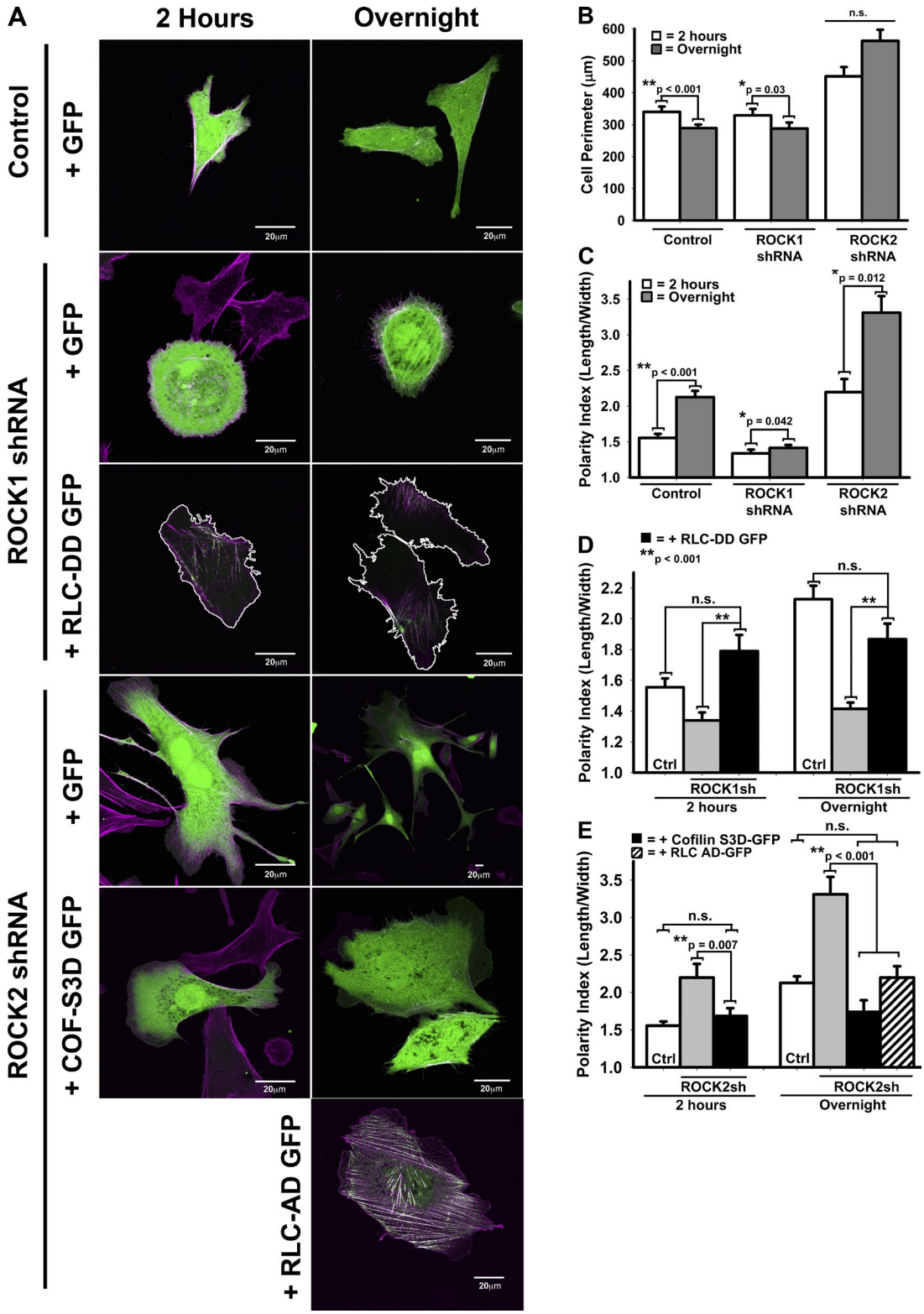

Figure 3. **ROCK1 and ROCK2 differentially regulate front–back polarity through isoform-specific mechanisms.** (A) Immunofluorescence of CHO.K1 cells cotransfected with either ROCK isoform–specific shRNA or control empty vector and the indicated GFP construct were plated on 2 μg/ml fibronectin for 2 h (left) or overnight (right), and actin filaments were stained with rhodamine phalloidin (magenta). ROCK1 shRNA cells coexpressing RLC-DD–GFP are outlined in white to indicate cell morphology. (B and C) Quantification of cell perimeter (B) and polarity index as measured by cell length divided by width (C), after 2 h or overnight plating on 2 μg/ml fibronectin; n = 39/106 control cells, 42/64 ROCK1 shRNA cells, and 26/89 ROCK2 shRNA cells (n = 2 h/overnight plating). (D) Quantification of polarity index in control cells (Ctrl; white bars) or ROCK1 shRNA cells coexpressing either GFP alone (gray bars) or RLC-DD–GFP (black bars); n = 39/42/33 cells at 2 h and n = 106/64/42 cells after overnight plating (n = control/ROCK1 shRNA + GFP/ROCK1 shRNA + RLC-DD–GFP). (E) Quantification of polarity index in control cells (white bars) or ROCK2 shRNA cells coexpressing either GFP alone (gray bars) or cofilin-S3D–GFP (black bars) or RLC-AD–GFP (diagonal stripes); n = 39/26/22 cells at 2 h and n = 106/89/12/44 cells after overnight plating (n = control/ROCK2 shRNA + GFP/ROCK2 shRNA + cofilin-S3D GFP/ROCK2 shRNA + RLC-AD GFP). Error bars indicate SEM.

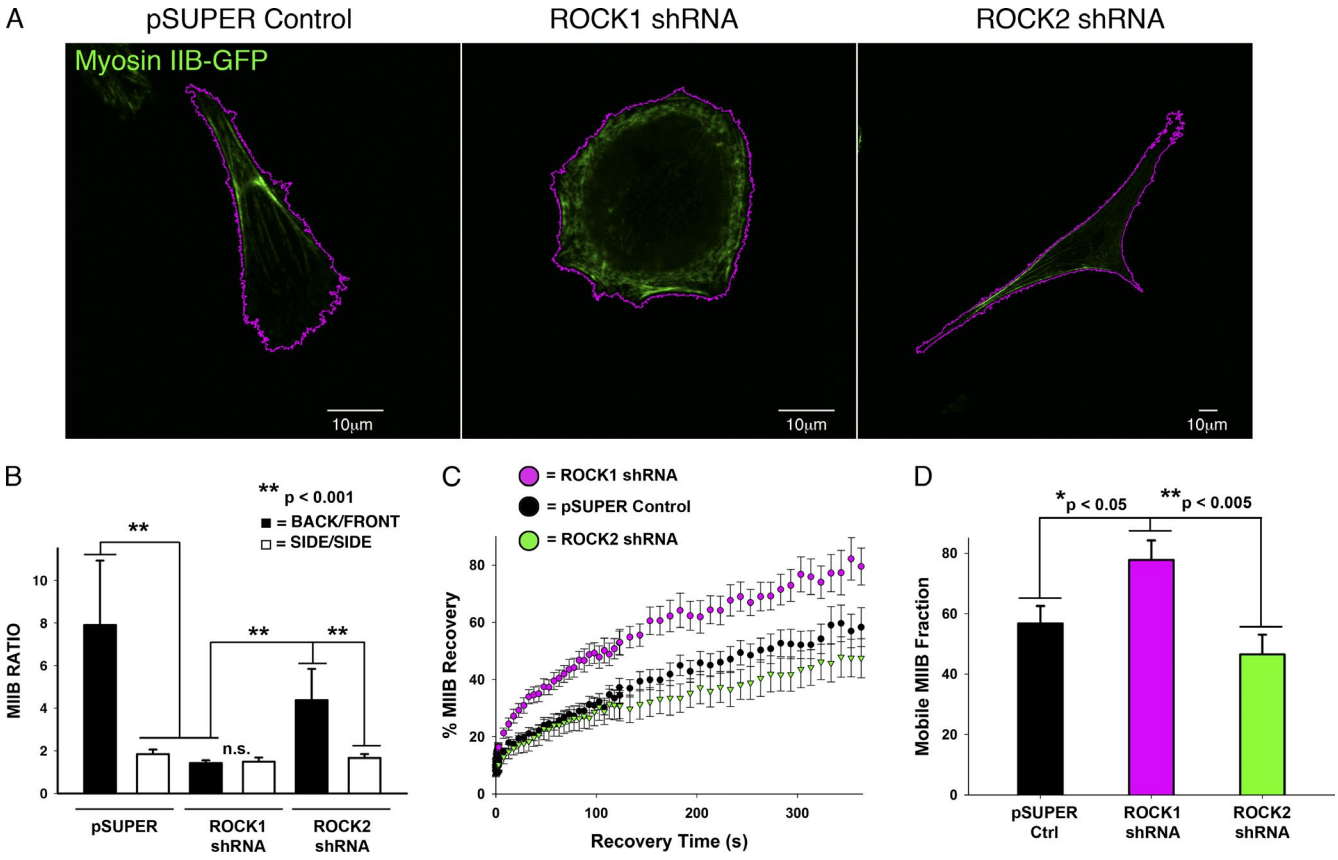

Figure 4. **ROCK1 generates actomyosin filament bundles that form the cell rear.** (A) Confocal images of CHO.K1 cells cotransfected with either ROCK isoform–specific shRNAs or pSUPER control empty vector and Myosin IIB–GFP (MIIB-GFP). The cell edge is outlined in magenta to indicate morphology. (B) Quantification of the ratio between integrated density for MIIB-GFP intensity at the rear (180° ± 90°) versus the front of the cell (0° ± 90°) and the ratio between the two sides of the cell (90° ± 90° and 270° ± 90°), where the integrated density = mean gray value × area. The numerator is defined as the side with increased MIIB-GFP intensity; *n* = 28 control cells, 21 ROCK1 shRNA cells, and 37 ROCK2 shRNA cells. (C) FRAP recovery curves for photobleached MIIB-GFP in ROCK shRNA and control cells. (D) MIIB mobile fraction calculated from FRAP recovery curves as the percentage of recovered MIIB fluorescence intensity; *n* = 23 control cells, 13 ROCK1 shRNA cells, and 9 ROCK2 shRNA cells for FRAP data in C and D. Error bars indicate SEM. Ctrl, control.

2011; Vicente-Manzanares and Horwitz, 2010). ROCK1 depletion resulted in round, nonpolar cells, which lacked large actomyosin filament bundles; instead, they exhibited short MIIB-decorated actin filaments around the periphery of the cell (Fig. 4, A and B; and Fig. S4). In contrast, ROCK2 knockdown and control cells exhibited MIIB preferentially localized in actomyosin filament bundles that defined the sides and rear of the polarized cell (Fig. 4 A and Fig. S4), although ROCK2 did affect the localization of MIIA within protrusions (Fig. S4). Phalloidin-labeled actin filaments displayed a similar pattern. Additionally, FRAP of MIIB filaments in ROCK1-deficient cells revealed an increase in the MIIB mobile fraction, indicating decreased MIIB affinity for the actomyosin bundles (Fig. 4, C and D). These results demonstrate that ROCK1 increases the affinity of MIIB for actin filaments consistent with previous measurements of MIIB turnover in the presence of diphosphorylated RLC (Vicente-Manzanares and Horwitz, 2010).

Mature dendritic spines in neurons are also enriched in actomyosin filaments (Matus et al., 1982; Morales and Fifková, 1989). Y-27632–mediated ROCK inhibition results in filopodia-like spine precursors, which fail to mature with time or in response to excitatory stimulation (Hodges et al., 2011). In contrast, ROCK-mediated RLC T18, S19 diphosphorylation promotes spine maturation into a polarized mushroom shape (Hodges et al., 2011). We hypothesized that if ROCK1 is the primary isoform responsible for RLC diphosphorylation in postsynaptic spines, specific knockdown of ROCK1 should result in filopodia-like spine precursors. In the absence of ROCK1, but not ROCK2, we observed long, thin filopodia-like spine precursors (Fig. 5, A–C), which lacked RLC T18, S19 diphosphorylation (Fig. 6 A) and failed to form synapses with VGlut-1/synaptophysin-labeled presynaptic terminals (Fig. 5 A and Fig. 6 B). In response to glycine-mediated excitatory stimulation (Park et al., 2004), ROCK1 knockdown spines failed to mature into a polarized mushroom shape with a clear spine head (Fig. 5, E and F). Furthermore, ROCK1 knockdown resulted in a dramatic loss of actin enrichment in spines, as assayed by ratio of fluorescence intensity of phalloidin-labeled actin filaments in the spine to those in adjacent dendrites (Fig. 6, B and C). Expression of phosphomimetic RLC-T18D, S19D rescued spine actin enrichment and synapse formation in the ROCK1 knockdown neurons (Fig. 6, B and C). Thus, ROCK1-mediated RLC diphosphorylation drives spine maturation into a polarized mushroom shape as well as front–rear polarity in migratory fibroblasts.

ROCK2 attenuates Rac1 activity at the leading edge and dendritic spine head

The loss of polarity observed in ROCK1 knockdown cells could result from concomitant up-regulation of Rac1 activity

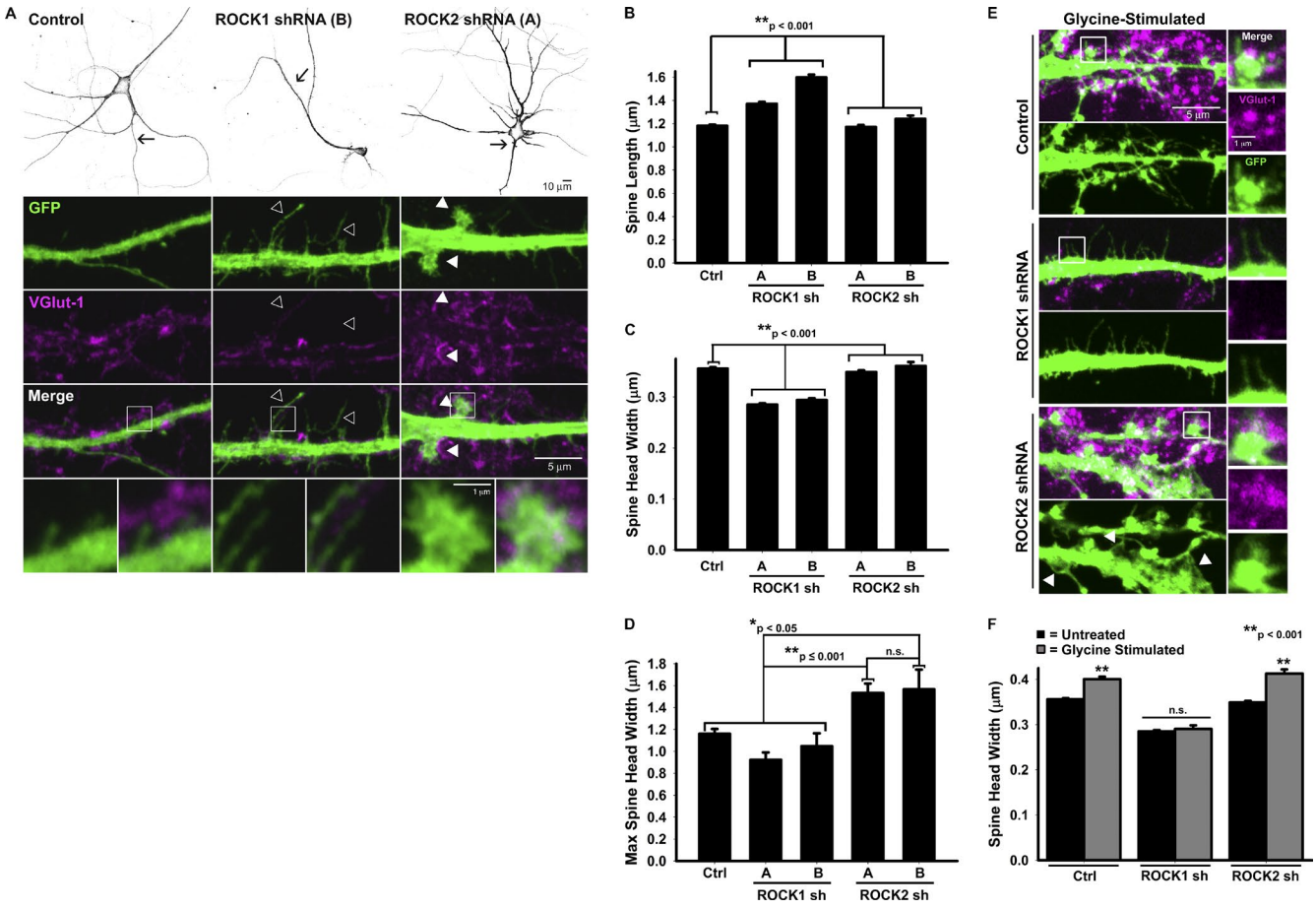

Figure 5. **ROCK1 and ROCK2 differentially regulate dendritic spine morphology in development and in response to excitatory stimulation.** (A) Confocal images of DIV19 fixed rat hippocampal neurons cotransfected with control empty vector or ROCK isoform–specific shRNAs and GFP on DIV 16, and stained for the presynaptic marker VGlut-1. (bottom) Enlargement of ROI indicated in merge images, highlighting dendritic spines and associated presynaptic VGlut-1 labeling. Neurons transfected with two other rat ROCK isoform-specific sequences are shown in Fig. S3. Arrows indicate the dendrite region of interest enlarged in the panels below the neuron image. Open arrowheads indicate immature filopodia-like spine precursors in ROCK1 knockdown neurons, whereas closed arrowheads indicate the presence of enlarged spine heads in ROCK2 knockdown neurons. (B–D) Quantification of spine length (B), spine head width (C), and max spine head width (D) per neuron in DIV19–23 rat hippocampal neurons; $n \geq 773$ spines for all conditions; for max spine head width calculation, $n = 38$, 19, 31, 13, and 6 neurons for control, ROCK1 shRNA sequence A, ROCK1 shRNA sequence B, ROCK2 shRNA sequence A, and ROCK2 shRNA sequence B. (E) Confocal images of dendrites from DIV23 rat hippocampal neurons after *N*-methyl-D-aspartate receptor activation with 200 µM glycine. Arrowheads indicate lamellipodia-like veils in glycine-stimulated ROCK2 shRNA neurons. (F) Quantification of spine head width in untreated and glycine-stimulated neurons; $n \geq 442$ spines for all conditions. Error bars indicate SEM. Ctrl, control.

in response to decreased myosin II activity, i.e., mechanotransduction. However, cells expressing constitutively active Rac1 exhibit a different phenotype—large lamellipodia and membrane ruffles around the cell (Ridley et al., 1992), whereas ROCK1-deficient CHO.K1 cells exhibit membrane retractions, similar to ROCK1-deficient prostate cancer cells (Vega et al., 2011). Indeed, fluorescence resonance energy transfer (FRET)–based wild-type (WT) Raichu Rac1 confirmed that Rac1 activity was not elevated in ROCK1 knockdown cells when compared with controls (Fig. 7, A and B). However, we did observe a 10% increase in Rac1 activity in ROCK2-deficient cells as measured by FRET (Fig. 7, A and B). Y-27632 treatment elevated Rac1 activity in ROCK1 knockdown cells by ∼10% but did not increase Rac1 activity in ROCK2-deficient cells, further demonstrating that ROCK2 is the primary isoform responsible for attenuating Rac1 activity (Fig. 7 B). Elevated Rac1 activity in ROCK2-deficient cells was also observed by pull-down of activated Rac1 with the p21-activated kinase (PAK)–protein binding domain (PBD) domain (Fig. 7 C; Glaven et al., 1999), consistent with previous measurements of increased Rac1 activity in Y-27632–treated cells (Katsumi et al., 2002); however, coexpression of monophosphomimetic RLC-T18A, S19D restored Rac activity to control levels (Fig. 7 C).

Whereas Rac1 activity mediates formation of the leading edge in migratory fibroblasts, it similarly drives actin polymerization to form the dendritic spine head in neurons (Tashiro and Yuste, 2004; Fortin et al., 2010). Unlike knockdown of ROCK1, spines in ROCK2 knockdowns are enriched for actin and diphosphorylated myosin RLC (Fig. 6) and form synapses (Fig. 5 A and Fig. 6 B). However, a fraction of ROCK2 knockdown spines display significantly enlarged spine heads (Fig. 5 D). Similar to CHO.K1 cells, postsynaptic compartments in ROCK2-deficient neurons exhibited a ∼10% increase in Rac1 activity as measured by FRET when compared with control neurons (Fig. 7, D and E). Furthermore, in response to glycine-mediated stimulation, ROCK2-deficient neurons exhibit lamellipodia-like veils reminiscent of constitutively active Rac1 (Fig. 5 E, arrowheads; Tashiro et al., 2000; Zhang and Macara, 2006). Thus, ROCK2 regulates Rac1 activity in both

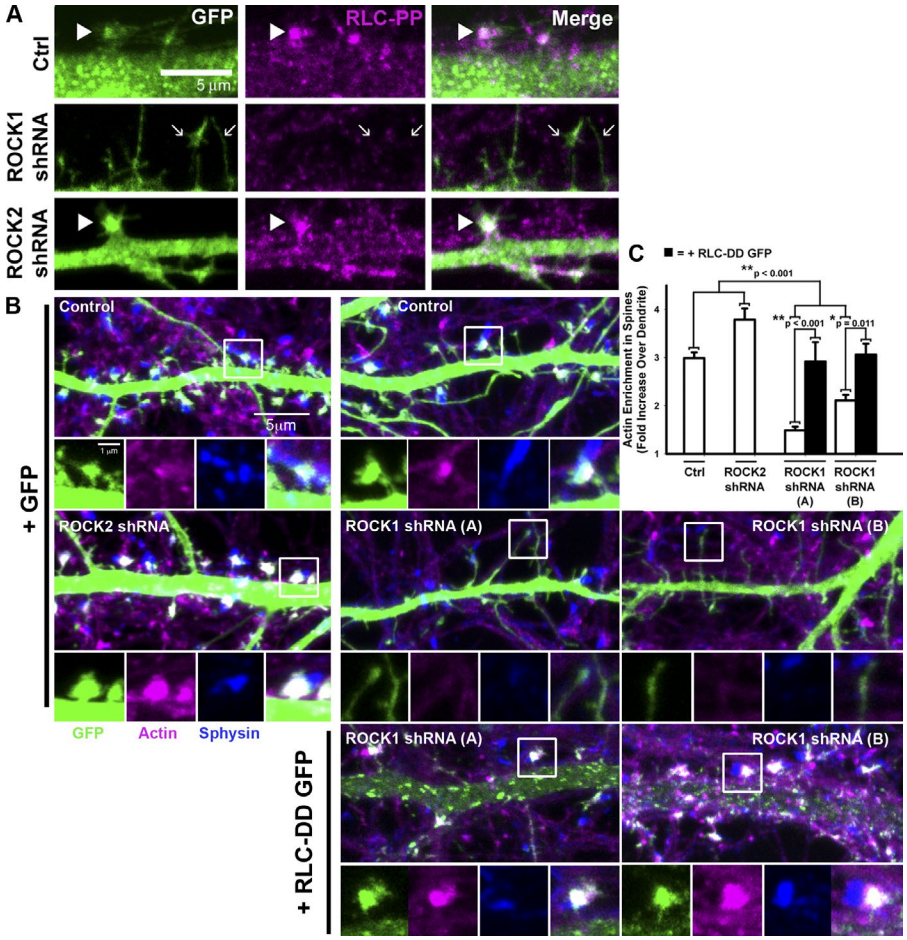

Figure 6. **Diphosphomimetic RLC-T18D, S19D rescues spine actin enrichment and synapse formation in ROCK1 knockdown neurons.** (A) DIV 19 rat hippocampal neurons were fixed and stained for diphosphorylated RLC (RLC-PP). Arrowheads indicate RLC-PP enrichment in postsynaptic spines of control and ROCK2 knockdown neurons, whereas arrows highlight the lack of RLC-PP in spines of ROCK1 knockdown neurons. (B) DIV 22 rat hippocampal neurons were fixed and stained for actin with rhodamine phalloidin (magenta) and the presynaptic marker, Synaptophysin (Sphysin). Control neurons (top) and ROCK2 knockdown neurons (sequence A) exhibit actin-enriched spines that colocalize with the presynaptic marker, Synaptophysin. ROCK1 knockdown neurons exhibit a loss of spine actin enrichment and synapse formation that was rescued by coexpressing diphosphomimetic RLC-T18D, S19D-GFP (bottom). (C) Quantification of spine actin enrichment, quantified as the ratio of the mean intensity of rhodamine phalloidin in spines to the mean intensity in the adjacent dendrite segment. Actin enrichment was calculated for $n \geq 40$ spines for all conditions. Error bars indicate SEM. Ctrl, control.

CHO.K1 migratory fibroblasts and dendritic spines to form the leading edge and expanded spine head, respectively.

ROCK2 generates contractile forces that inversely correlate with Rac activity

Inhibition of both ROCK isoforms with Y-27632 decreases contractile forces (Yee et al., 2001; Beningo et al., 2006). However, to determine whether both ROCK1-mediated RLC diphosphorylation and ROCK2-mediated RLC monophosphorylation generate contractile forces, we used traction force microscopy with isoform-specific knockdowns of either ROCK1 or ROCK2. The mean stress, calculated as the mean force per cell area, was similar between control and ROCK1 knockdown cells. However, knockdown of ROCK2 significantly reduced mean stress per cell, which could be rescued by coexpression of monophosphomimetic RLC-T18A, S19D (Fig. 8 C). Additionally, control CHO.K1 cells plated overnight exhibit maximum forces along the front–rear axis of the cell and decreased forces at the sides of the cell (Fig. 8 D), consistent with myosin II–mediated transmission of contractile forces generated within protrusions to the cell rear, where actomyosin filament bundles are stabilized. Unlike control cells, ROCK2-deficient cells exhibit increased forces at the cell rear, but not at the front of the cell (Fig. 8 E), suggesting that ROCK2-mediated RLC monophosphorylation generates contractile forces at the leading edge of the cell. Coexpression of monophosphomimetic RLC-T18A, S19D restored forces at the front of the cell to control levels (Fig. 8 E; also see Fig. 8 B, force distribution).

Although ROCK1 knockdown cells exhibit forces similar to control cells, their round morphology suggests the loss of polarized contractile forces. Both control and ROCK2 knockdown cells exhibit polarized force gradients, with the cell rear exhibiting significantly higher forces than the sides of the cell (Fig. 8 F). In contrast, ROCK1 knockdown resulted in uniform forces around the cell (Fig. 8, C–F), mirroring the uniform distribution of short actomyosin filaments around the cell periphery (Fig. 8 A). Thus, ROCK1-mediated RLC diphosphorylation stabilizes actomyosin filament bundles, resulting in polarized contractile forces at the rear of the cell.

In addition to forming the rear of the cell, RLC diphosphorylation also polarizes Rac1 activity to the front of migrating cells (Vicente-Manzanares et al., 2011). To determine whether ROCK1 is required for this polarized Rac1 activity, we combined traction force microscopy and Rac1 activity measurements, as assayed by WT-Raichu Rac1 FRET. As a control, we expressed the constitutively active Raichu Rac1 V12 FRET probe, which results in a uniform FRET signal throughout the cell (Fig. 9 B, gray bars). Using the WT Raichu Rac1 FRET probe, both control and ROCK2-deficient cells polarized Rac1 activity away from the location of maximum force (Fig. 9, A and B, black bars); whereas ROCK1-deficient cells showed uniformly distributed Rac1 activity around the perimeter of the cell (Fig. 9, A and B), implicating stabilized contractile forces at the cell rear in the polarized localization of Rac1 activity to the front of the cell.

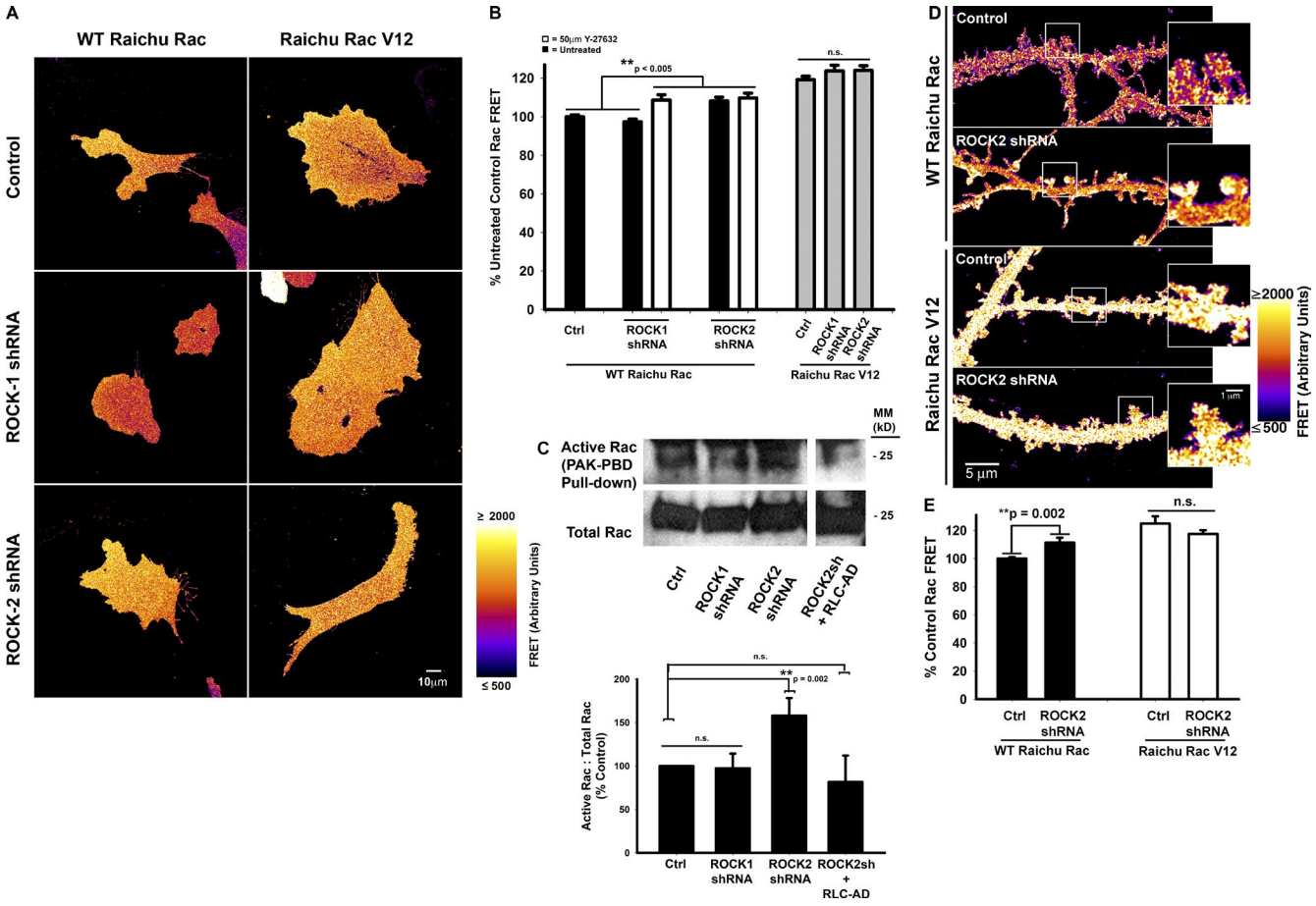

Figure 7. **ROCK2 attenuates Rac activity underlying the formation of protrusions in migratory cells and the spine head of neurons.** (A) Ratiometric images of FRET to CFP donor intensity in CHO.K1 cells expressing either the WT Raichu Rac FRET probe or as a positive control, the constitutively active Raichu Rac V12. (B) Quantification of ratiometric FRET intensity normalized to control WT Raichu Rac values; gray bars, untreated Raichu Rac V12. $n \geq 30$ cells for all conditions. (C) Western blot and analysis of active Rac pulled down with PAK-PBD beads in CHO.K1 lysates, and Rac in the total lysate (bottom) similarly shows increased Rac activation in the ROCK2 knockdown cells, which is restored to control levels with coexpression of RLC-T18A, S19D (RLC-AD); $n = 6$ control [Ctrl], 5 ROCK1 shRNA, 6 ROCK2 shRNA, and 3 ROCK2 shRNA + RLC-AD. (D) Ratiometric images of FRET to CFP donor intensity in postsynaptic dendrites and spines of DIV 23 rat hippocampal neurons expressing either the WT Raichu Rac FRET probe or as a positive control, the constitutively active Raichu Rac V12. (E) Quantification of ratiometric FRET intensity normalized to control WT Raichu Rac values; black bars, WT Raichu Rac; white bars, Raichu Rac V12. ROCK2 knockdown increases postsynaptic Rac FRET similar to CHO.K1 cells. *n* (WT Raichu Rac) = 15 control and 10 ROCK2 shRNA neurons; *n* (Raichu Rac V12) = 12 control and 9 ROCK2 shRNA neurons. Error bars indicate SEM. MM, molecular mass.

ROCK-2–mediated cofilin inactivation regulates adhesion and PSD size

In response to myosin II–driven contractile forces, adhesions elongate and mature along actin filaments (Parsons et al., 2010). Adhesion maturation also correlates inversely with Rac1 activity (Kuo et al., 2011). Interestingly, both ROCK knockdowns result in significantly smaller adhesions than control cells, with ROCK2 knockdowns exhibiting adhesion sizes intermediate between control and ROCK1 knockdown cells (Fig. 10 B). Notably, ROCK2 shRNA cells, unlike ROCK1-depleted cells, exhibit mature adhesions associated with large actomyosin filament bundles (Fig. 10 A), demonstrating that adhesions that do mature are stabilized by actomyosin filament bundles in ROCK2 knockdown cells. Similar to control cells, these mature adhesions in ROCK2 knockdown cells require stable actomyosin bundles, as demonstrated by using nonphosphorylatable RLC-T18A, S19A to disrupt actomyosin filament contraction and bundling. RLC-AA reduced adhesion size in both control and ROCK2 knockdown cells, but not ROCK1 knockdown cells (Fig. 10 C). Furthermore, expression of phosphomimetic RLC T18D, S19D rescued adhesion size in ROCK1 knockdown cells and elevated adhesion size in control and ROCK2 knockdown cells to similar levels (Fig. 10 D), demonstrating that stable actomyosin filament bundles generated by RLC diphosphorylation support adhesion maturation. Using total internal reflection (TIRF) microscopy, paxillin-labeled adhesions in ROCK1-deficient cells initially mature within protrusions, but maturation stops abruptly at the lamellar interface (Video 3), consistent with persistence of ROCK2-driven contractile forces, but absence of ROCK1 mediated actomyosin filament bundles needed to stabilize mature adhesions at the cell rear. Stabilization of mature adhesions at the cell rear could be rescued by coexpressing RLC-DD–GFP in ROCK1-deficient cells (Video 4).

In addition to myosin activity, inactivation of cofilin-mediated actin severing by expression the phosphomimetic mutant, cofilin-S3D, rescued adhesion size in ROCK2 knockdown cells and further increased adhesion size in control and ROCK1 knockdown cells (Fig. 10 E). Using TIRF to visualize adhesions in protrusions, ROCK2 knockdown cells exhibit small nascent adhesions that fail to enlarge (Video 1), but expression of co-

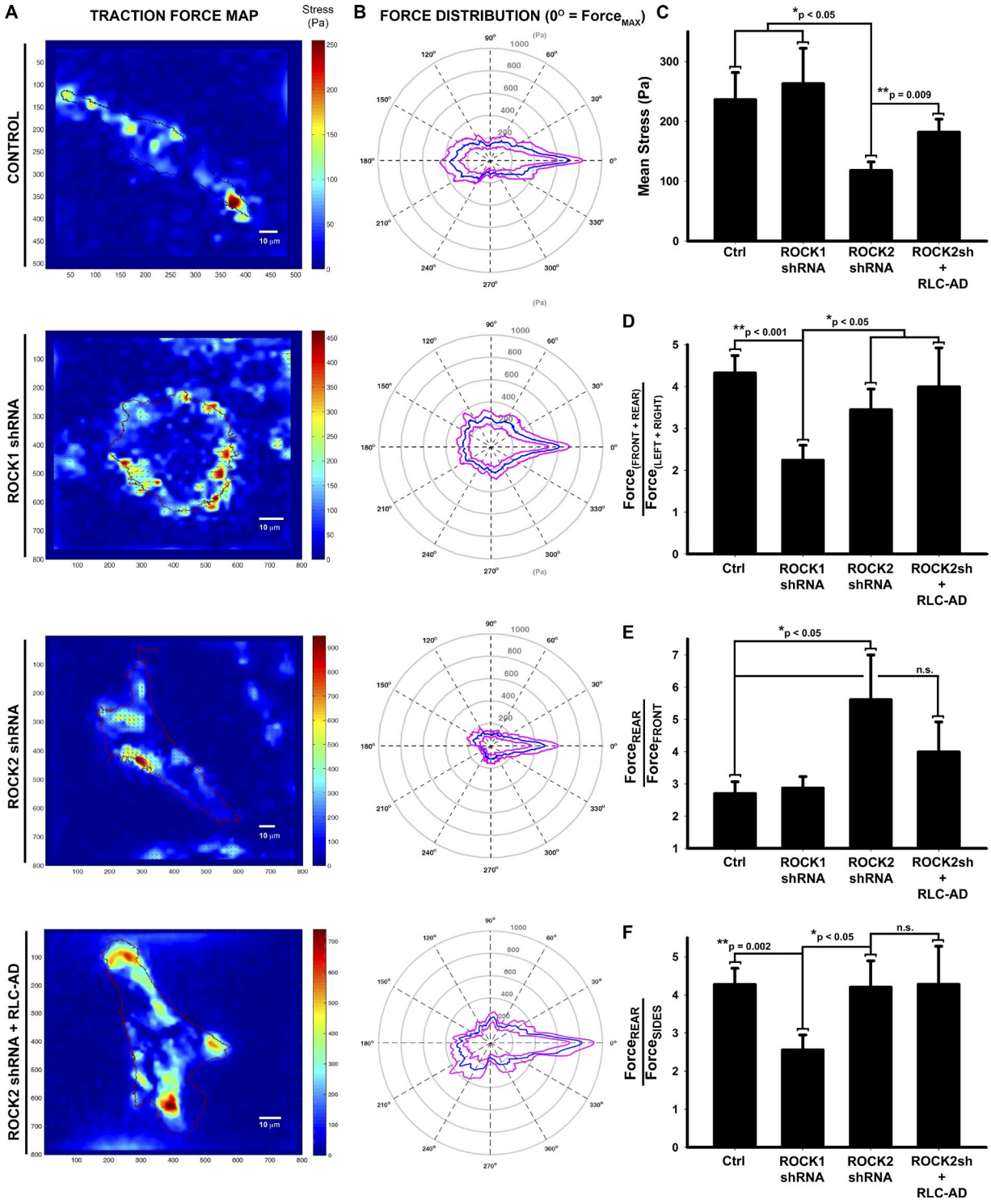

Figure 8. **ROCK2 generates contractile forces at the front of the cell.** (A) Force maps of control and ROCK shRNA CHO.K1 cells plated overnight on fibronectin-coated 5-kPa polyacrylamide gels. (B) Angular force diagrams display the maximum force for each 0.5°, where 0° corresponds to the location of maximum force, or the rear of the cell. The blue line represents the mean value for all cells ± the standard error (magenta lines). (C) Quantification of mean stress (kPa) in ROCK knockdown and control cells. (D) Quantification of the ratio of forces along the front–rear axis to forces along the sides of the cell, where the rear of the cell is defined as 0°, the location of maximum force. (E) Quantification of the ratio of forces at the rear of the cell (0°) to forces at the front of the cell (180°). (F) Quantification of the ratio of forces at the rear of the cell (0°) to forces at the sides of the cell (maximum force of 90° or 270°). n = 28 control cells, 23 ROCK1 shRNA cells, 27 ROCK2 shRNA cells, and 14 ROCK2 shRNA + RLC-AD–GFP cells. Error bars indicate SEM. Ctrl, control.

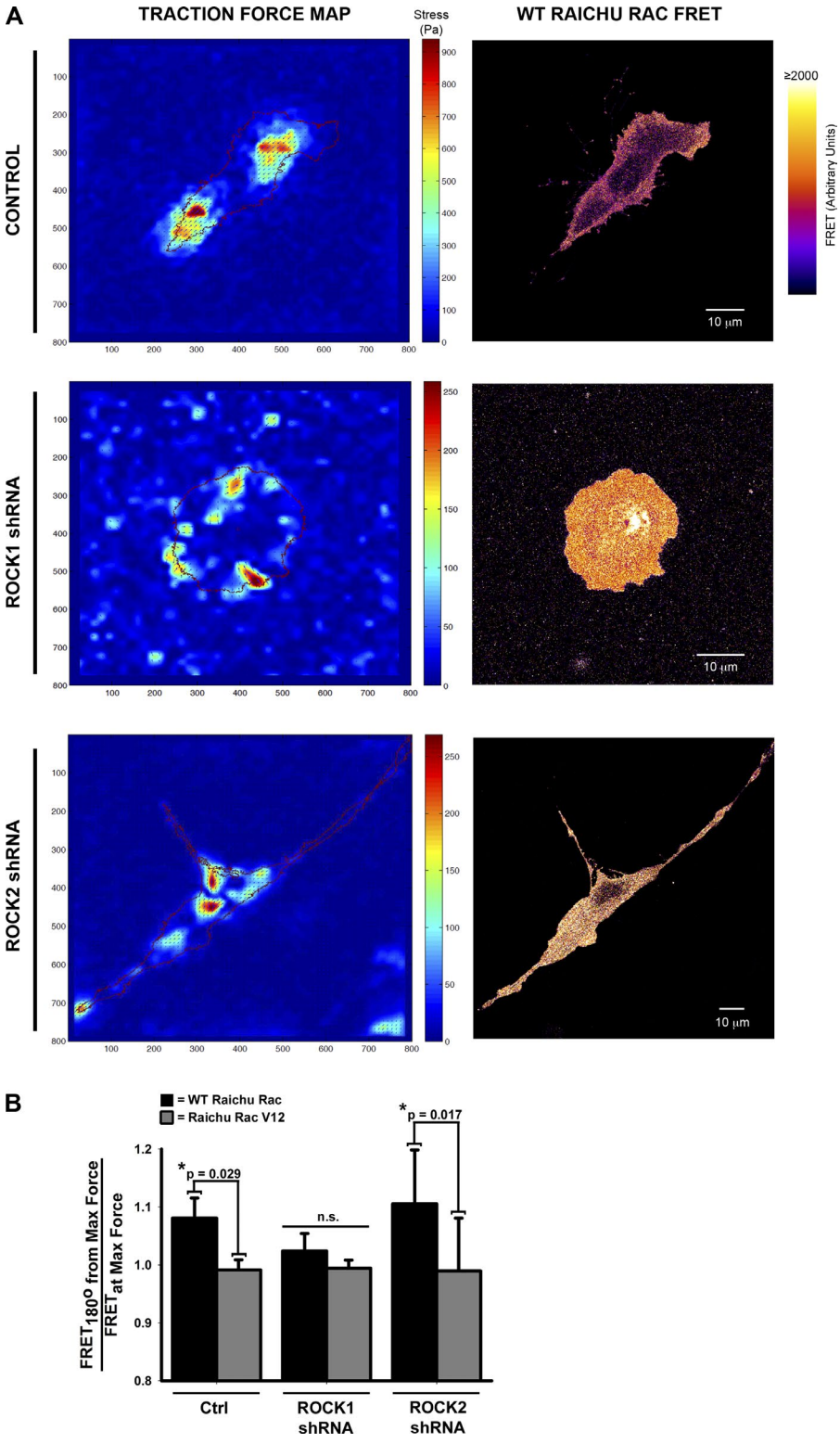

Figure 9. **ROCK1 polarizes Rac activity to the front of the cell.** (A) Force diagrams and corresponding FRET ratiometric images for control and ROCK shRNA CHO.K1 cells plated overnight on fibronectin-coated 5-kPa polyacrylamide gels. (B) Quantification of Rac FRET at the front of the cell (180° from maximum) versus at the rear of the cell (0° = location of max force) for control and ROCK shRNA CHO.K1 cells. The constitutively active control, Raichu Rac V12, exhibits a uniform FRET signal throughout the cell, resulting in a ratio of ~1. *n* = 6/8 control cells, 6/4 ROCK1 shRNA cells, and 7/7 ROCK2 shRNA cells, in which *n* = WT Raichu Rac/Raichu Rac V12. Error bars indicate SEM. Ctrl, control.

filin-S3D–GFP rescued adhesion maturation (Video 2). These results suggest that ROCK2 initiates adhesion elongation along actin filaments within protrusions, but ROCK1-mediated RLC diphosphorylation drives subsequent adhesion maturation and polarizes mature adhesions toward the cell rear.

Because ROCK2-mediated cofilin phosphorylation regulates adhesion size, we assessed whether cofilin-mediated actin remodeling also regulates the size of the PSD, which can be viewed as another kind of adhesion. We have already demonstrated that myosin II activity regulates PSD size analogously to that of adhesion maturation (Hodges et al., 2011). Similarly, expression of cofilin-S3D drives PSD enlargement in DIV14 neurons when compared with either control or cofilin S3A–expressing neurons (Fig. 10, F and G), demonstrating that ROCK2-mediated cofilin inactivation regulates both cell–matrix adhesion and PSD size. Notably, active cofilin S3A did not

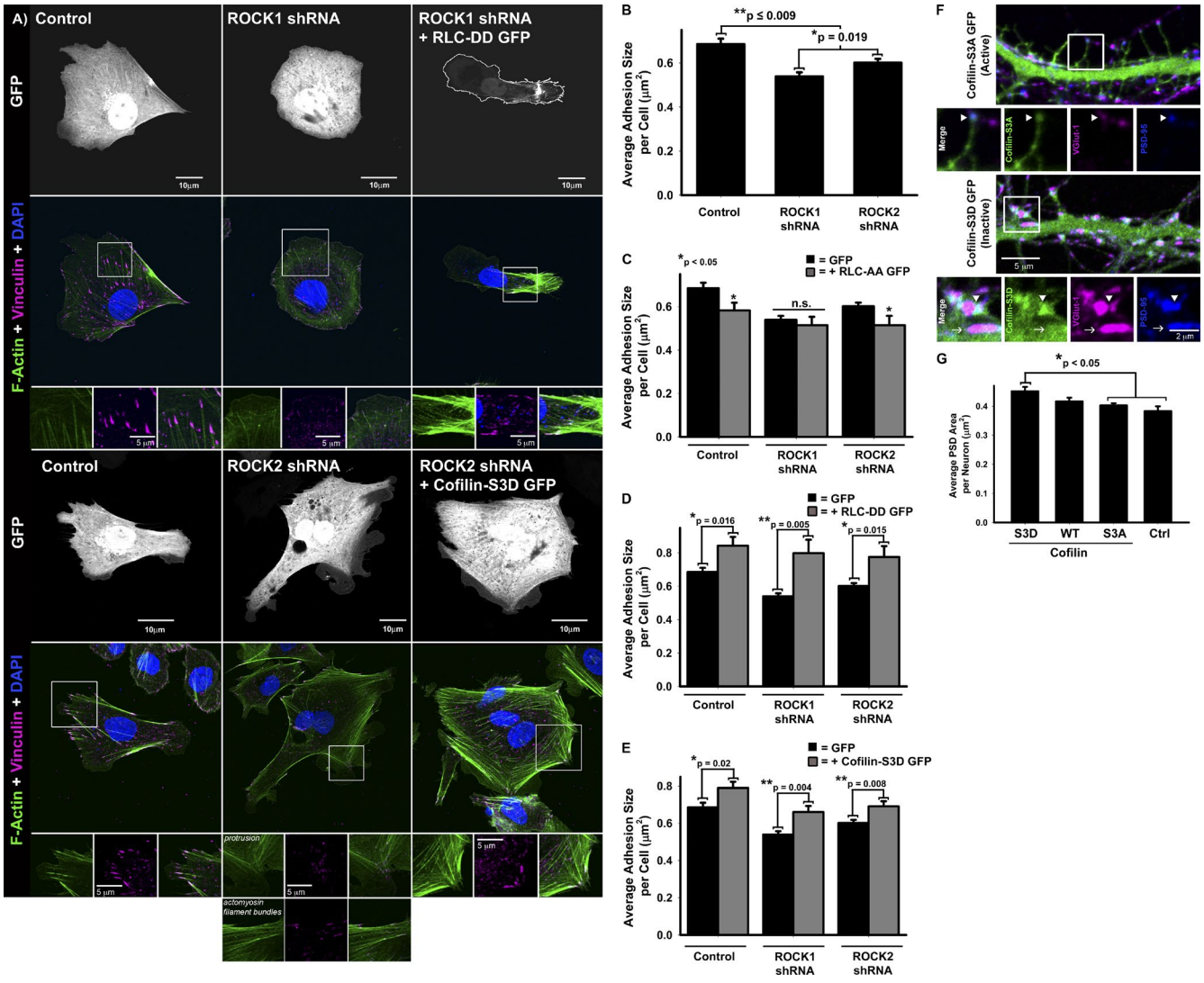

Figure 10. **RLC T18, S19 diphosphorylation and cofilin S3 phosphorylation regulate adhesion and PSD maturation.** (A) Knockdown of either ROCK1 or ROCK2 reduces adhesion size but can be rescued by coexpression of either diphosphomimetic RLC-T18D, S19D or phosphomimetic cofilin S3D, respectively. CHO.K1 cells cotransfected with either control empty vector or ROCK shRNAs and the indicated GFP construct and plated on 2 µg/ml fibronectin for 2 h were stained for actin and the adhesion marker vinculin. (B) Quantification of mean adhesion size per cell. (C) Nonphosphorylatable RLC-T18A, S19A significantly reduces adhesion size in control and ROCK2 knockdown cells, but not ROCK1 knockdown cell. Quantification of mean adhesion size per cell in CHO.K1s expressing GFP or GFP-tagged RLC-T18A, S19A (RLC-AA–GFP). (D) Diphosphomimetic RLC-T18D, S19D rescues adhesion size in ROCK1 shRNA cells and increases adhesion size in control and ROCK2 shRNA cells. Quantification of mean adhesion size per cell in CHO.K1s expressing either GFP or GFP-tagged RLC-T18D, S19D (RLC-DD–GFP). (E) Phosphomimetic cofilin S3D rescues adhesion size in ROCK2 shRNA cells, but also increases adhesion size in control and ROCK1 shRNA cells. Quantification of mean adhesion size per cell in CHO.K1s expressing either GFP or GFP-tagged cofilin S3D. *n* for adhesion analysis ≥ 9 cells per condition with a mean of >100 adhesions analyzed per cell. (F) Cofilin inactivation increases PSD size. Immunofluorescence of DIV 14 rat hippocampal neurons transfected with either the active, nonphosphorylatable cofilin-S3A–GFP or the inactive phosphomimetic mutant, cofilin-S3D–GFP, and costained for the presynaptic marker, VGlut-1, and postsynaptic marker, PSD-95. Arrowheads indicate synapses in the two conditions. Arrows indicate a dendritic, as opposed to spine-associated, synapse, in a cofilin-S3D–expressing neuron. (G) Quantification of mean PSD area per neuron in rat hippocampal neurons expressing either GFP (control [Ctrl]) or GFP-tagged cofilin constructs (S3A, WT, and S3D). *n* = 12 cofilin S3D-expressing neurons, 11 cofilin S3A-expressing neurons, 12 WT cofilin-expressing neurons, and 5 control neurons. Error bars indicate SEM.

noticeably affect PSD size, consistent with research suggesting that cofilin phosphorylation precedes PSD enlargement (Bosch and Hayashi, 2012). All of this supports the notion that actin filament integrity and organization drive PSD size and morphology similar to adhesions (Parsons et al., 2010).

Discussion

We have demonstrated that ROCK1 and ROCK2 differentially regulate actomyosin organization and cell polarity using two different cellular systems—dendritic spine polarity in neurons and front–back polarity in migratory cells. Although ROCK1 and 2 exhibit differential tissue expressions, with ROCK2 specifically enriched in neuronal tissues (Leung et al., 1996; Matsui et al., 1996; Nakagawa et al., 1996), we observed strikingly similar contributions of ROCK1 and ROCK2 to the polarity of migrating cells and postsynaptic dendritic spines in neurons.

In both systems, ROCK1 initiates polarity through the formation of stable actomyosin filament bundles, whereas ROCK2 generates contractile forces and locally attenuates Rac1 activity creating a polarity that leads to the formation of the leading

edge in migratory cells and spine head in neurons. Through this study, we have dissected both the underlying, shared molecular pathways of migratory and dendritic spine polarity and revealed novel ROCK isoform-specific roles in synaptic plasticity.

In parsing the different activities of ROCK isoforms, we identified a ROCK1-specific mechanism that supports cell polarity. Specifically, ROCK1 diphosphorylates myosin RLC to activate myosin II (Vicente-Manzanares et al., 2008), polarizing contractile forces and establishing an inverse Rac1 activity gradient, which segregates actin polymerization to the leading edge (Vicente-Manzanares et al., 2011). We demonstrate that ROCK1-mediated RLC diphosphorylation generates actomyosin filament bundles but does not generate contractile forces. This is consistent with in vitro measurements of smooth muscle myosin, which, similar to nonmuscle myosin II, is regulated by phosphorylation on residues Thr18 and Ser19 (Vicente-Manzanares et al., 2009) and in which RLC diphosphorylation increases myosin ATPase activity in comparison with RLC S19 monophosphorylation but does not further increase myosin contractility as measured by the in vitro velocity of actin filaments (Umemoto et al., 1989). We and others have previously shown that these actomyosin filament bundles resulting from RLC diphosphorylation form both the sides and rear of migrating cells and the mushroom-shaped morphology characteristic of mature dendritic spines (Kolega, 2003; Ryu et al., 2006; Vicente-Manzanares et al., 2008; Hodges et al., 2011). Additionally, although ROCK1 localizes Rac activity to the leading edge, it does not affect the overall magnitude of Rac activity. This unites previous observations that RLC diphosphorylation inhibits local Rac signaling, thereby polarizing activators of Rac signaling to the leading edge (Vicente-Manzanares et al., 2011), but that ROCK2 generates contractile forces that inversely correlate with the magnitude of Rac activation (Katsumi et al., 2002). Finally, the absence of polarized actomyosin filament bundles in ROCK1-deficient cells also altered the organization of microtubules in fibroblasts, supporting evidence that actomyosin filament bundles initiate front–rear migratory cell polarity (Vicente-Manzanares et al., 2011). By comparison with migratory cell polarity, the morphology of dendritic spines depends largely on the actomyosin cytoskeleton, although microtubules transiently enter spines to regulate actin cytoskeletal dynamics, particularly in response to excitatory stimulation (Jaworski et al., 2009; Merriam et al., 2011). Because similar ROCK-mediated actomyosin organization underlies polarity in both systems, dendritic spines provide further evidence that ROCK1-driven actomyosin filament bundles initiate polarity.

Although ROCK1 creates the cell rear, ROCK2 specifically regulates formation of the leading edge of migratory cells and dendritic spine head of neurons. Consistent with this role, unlike ROCK1, which localizes almost exclusively to actomyosin filament bundles at the sides and rear of the cell, ROCK2 additionally localizes to protrusions, reconciling previous studies attributing ROCK2 localization to either actomyosin filament bundles (Katoh et al., 2001; Kawabata et al., 2004) or membrane protrusions and ruffles (Leung et al., 1995; Vega et al., 2011). This position uniquely situates ROCK2 to regulate both actin dynamics and myosin-mediated contractility within protrusions, which it does by phosphorylating cofilin at Ser3 and RLC at S19. ROCK2 generates contractile forces at the front of the cell through RLC S19 monophosphorylation, which has been shown to increase MIIB affinity for actin filaments, albeit to a lesser extent than RLC diphosphorylation, and to drive the initial maturation of adhesions associated with protrusions (Fig. S2; Vicente-Manzanares and Horwitz, 2010). Furthermore, ROCK2 is the specific isoform that regulates the magnitude of Rac activation through RLC-S19 monophosphorylation, consistent with previous evidence that contractile forces decrease Rac activity (Katsumi et al., 2002), although ROCK2 could also regulate Rac activity via NMII-mediated localization of Rac guanine exchange factors (Shin et al., 2014). In addition to regulating myosin II–driven contractile force generation, ROCK2 also inactivates the actin-severing protein cofilin, via Ser3 phosphorylation, leading to increased adhesion and PSD size. We propose that cofilin inactivation results in stable actin filaments on which adhesions can elongate. This is consistent with previous observations in which either α-actinin–mediated actin cross-linking or Dia-driven actin filament growth can support adhesion maturation in the absence of myosin II–mediated contractility (Choi et al., 2008; Stricker et al., 2013). Thus, ROCK1 and 2 regulate distinct aspects of RhoA activity underlying front–back polarity, namely ROCK1 initiates cell polarity by stabilizing actomyosin filament bundles to form the cell rear, whereas ROCK2 produces contractile forces and inactivates cofilin-mediated actin remodeling to drive adhesion maturation correlating with decreased Rac activity (Kuo et al., 2011).

In dendritic spine maturation, RhoA and Rac1 exhibit temporal reciprocity analogous to that seen for front–back polarity in migrating cells (Machacek et al., 2009; Rex et al., 2009). In response to excitatory stimulation, RhoA initiates LTP formation, whereas Rac1 is subsequently activated later during LTP consolidation (Rex et al., 2009). These sequential activities result in RhoA-mediated spine neck formation and subsequent Rac1-driven spine head expansion, leading to a mushroom-shaped morphology (Tashiro and Yuste, 2004; Lynch et al., 2007; Hodges et al., 2011). Our observations demonstrate that the two ROCK isoforms distinctly regulate these phases of LTP consolidation. Although ROCK1 supports the formation of a polarized spine, ROCK2 regulates Rac activity and cofilin S3 phosphorylation, resulting in spine head and PSD expansion. Our observation that inactivation of cofilin-mediated actin remodeling also increases PSD size in neurons is consistent with previous studies that cofilin inactivation by S3 phosphorylation promotes spine maturation (Shi et al., 2009; Pontrello et al., 2012). In spines, phospho–cofilin S3 is a hallmark of LTP induction (Chen et al., 2007; Rex et al., 2009), and more recent evidence shows that active cofilin is initially recruited to spines after LTP but is subsequently inactivated by S3 phosphorylation coincident with spine head enlargement (Bosch et al., 2014; Calabrese et al., 2014). From this, we hypothesize that ROCK2 may act as a switch between these two modes of LTP consolidation, an initial RhoA-driven mechanism that initiates cell polarity and a subsequent Rac1-driven phase that drives spine head enlargement.

In summary, we have found isoform-specific functions for ROCK1 and 2 in two kinds of cellular polarity. These observations underscore the need for isoform-specific inhibitors to target RhoA/ROCK-mediated signaling pathways in diverse biological processes. In particular, RhoA/ROCK-mediated signaling pathways are increasingly implicated in synaptic disorders, such as autism and schizophrenia (Pinto et al., 2010; van Bokhoven, 2011; Krey et al., 2013) as well as in stem cell pluripotency and differentiation (Watanabe et al., 2007a). For example, brains from autistic patients show a failure to prune unwanted synapses, leading to hyperexcitability, whereas brains

from schizophrenic patients have fewer synapses (Penzes et al., 2011). Building on our finding that the two ROCK isoforms differentially regulate synaptic development, ROCK isoform-specific inhibitors could selectively regulate distinct critical periods during synaptic development. For example, specific ROCK1 inhibition could prevent overformation of synapses, and conversely, a ROCK2-specific inhibitor could drive spine formation and spine head expansion. In the case of stem cells, the decision to self-renew or differentiate appears to be driven by mechanotransduction leading to transcriptional changes (Mammoto et al., 2012). Because ROCK2 regulates contractile forces, it would be of interest to determine whether inhibition of both ROCK1 and 2 are necessary to prevent differentiation or whether inhibition of ROCK2 alone is sufficient to maintain pluripotency. All of this points to the importance of ROCK isoforms and the need for specific reagents to study them.

Materials and methods

Antibodies and reagents

Rabbit polyclonal antibodies for phosphorylated human myosin light chain S19 and diphosphorylated T18/S19 were purchased from Rockland Immunochemicals (600–401-416) and Cell Signaling Technology (3674), respectively. A mouse monoclonal antibody against chicken myosin light chain (clone MY21) was purchased from Sigma-Aldrich (M4401). All myosin light chain antibodies were used at a concentration of ∼1:200–1:500 for both immunofluorescence and Western blotting. Rabbit polyclonal antibodies for human cofilin and phosphorylated human cofilin S3 were purchased from Santa Cruz Biotechnology, Inc. (sc-33779) and Abcam (ab12866), respectively. Both cofilin antibodies were used at a concentration of ∼1:200–1:500 for Western blotting. Rabbit polyclonal antibodies for phosphorylated human MYPT1 (T696) and phosphorylated human LIMK1 (T508)/LIMK2 (T505) were purchased from Cell Signaling Technology and used at a concentration of 1:200–1:500 for Western blotting. A mouse monoclonal antibody (clone B-2) against GFP from *Aequorea victoria* was purchased from Santa Cruz Biotechnologies, Inc. (sc-9996) and used at a concentration of 1:1,000–1:5,000 for Western blotting. A mouse monoclonal antibody (clone B-5-1-2) against sea urchin α-tubulin was purchased from Sigma-Aldrich (T6074) and used at a concentration of 1:5,000 for Western blotting. Rabbit monoclonal antibodies against human ROCK-1 (clone EPR638Y; 04–1121) and rat ROCK-2 (clone A9W4; 04–841) were purchased from EMD Millipore and used at a concentration of 1:500 for Western blotting. A guinea pig polyclonal antibody against rat Vglut-1 was purchased from Synaptic Systems (135 304) and used at a concentration of 1:1,000 for immunofluorescence. A mouse monoclonal antibody (clone D-4) against human synaptophysin was purchased from Santa Cruz Biotechnology, Inc. (sc-17750) and used at a concentration of 1:1,000 for immunofluorescence. A mouse monoclonal antibody against human Rac1 was purchased from BD (610650). A mouse monoclonal antibody (clone hVin1) against human vinculin was purchased from Sigma-Aldrich (V9131) and used at a concentration of 1:500 for immunofluorescence. Rabbit polyclonal antibodies against the C termini of human NMHCII-A and -B were purchased from Covance/BioLegend and have been previously described (Vicente-Manzanares et al., 2008, 2011; Vicente-Manzanares and Horwitz, 2010). Except for GFP, all antibodies used in this study exhibit significant cross-reactivity with mammalian species. Rhodamine phalloidin and Acti-stain 488 were purchased from Cytoskeleton, Inc. Anti–mouse, anti–rabbit, and anti–guinea pig Alexa Fluor–conjugated secondary antibodies (488, 568, and 647) were purchased from Invitrogen. Calyculin A and Y-27632 were purchased from EMD Millipore and used at the concentrations indicated in Fig. 1 and Fig. 7. Tetrodotoxin and strychnine were purchased from Sigma-Aldrich and reconstituted in dH_2O.

Plasmids and shRNA sequences

Full-length mRFP1-rat ROCK2 cloned into a pcDNA3.1(+) vector under the control of a cytomegalovirus (CMV) promoter was provided by M. Baccarini (Max F. Perutz Laboratories, University of Vienna, Wien, Austria; Niault et al., 2009), and where noted, we replaced RFP with GFP by subcloning full-length rat ROCK2 into a pEGFP-C3 vector (Takara Bio Inc.), also under the control of a CMV promoter. Full-length GFP-mouse ROCK1 cloned into a pcDNA-DEST53 vector (Life Technologies) under the control of a CMV promoter was a gift from C. Marshall (The Institute of Cancer Research, London, England, UK) and has been previously described (Vega et al., 2011). Full-length rat cofilin-GFP cloned into a pEGFP vector (Takara Bio Inc.) under the control of a CMV promoter was provided by J. Condeelis (Albert Einstein College of Medicine, Bronx, NY), and published S3A and S3D mutations (Agnew et al., 1995; Moriyama et al., 1996) were generated by site-directed PCR mutagenesis. Full-length human MHC-IIB–GFP (MIIB-GFP) cloned into a pEGFP-C3 vector (Takara Bio Inc.) under the control of a CMV promoter was from R.S. Adelstein (National Heart, Lung, and Blood Institute, National Institutes of Health, Bethesda, MD; Wei and Adelstein, 2000), and in this study, we used an shRNA-insensitive variant constructed by site-directed mutagenesis of TCAAGC, resulting in a silent mutation (Ser-Ser; Vicente-Manzanares et al., 2007). Both WT chicken RLC-GFP and RLC T18D, S19D-GFP (RLC-DD–GFP) were cloned into a pEGFP-N1 vector (Takara Bio Inc.) under the control of a CMV promoter and were provided by K. Kelly (National Cancer Institute, Bethesda, MD). RLC T18A, S19A-GFP (RLC-AA–GFP) was generated by site-directed PCR mutagenesis of the WT construct (Vicente-Manzanares et al., 2008). Full-length chicken paxillin-GFP cloned into the pEGFP-N3 vector (Takara Bio Inc.) under the control of the CMV promoter has been described previously (Laukaitis et al., 2001), and where noted, GFP was replaced by mOrange from R. Tsien (University of San Diego, San Diego, CA; Shaner et al., 2004). The WT Raichu Rac and constitutively active Raichu Rac G12V (V12) FRET probes were provided by M. Matsuda (Osaka University, Osaka, Japan; Itoh et al., 2002) and consist of YFP, the CRIB domain of human PAK1 (amino acids 68–150), human Rac1 (amino acids 1–176), and CFP cloned into a derivative of the pCAGGS vector (Niwa et al., 1991). GST-PBD, used in the active Rac pull-down assay, was provided by M. Schwartz (Yale University, New Haven, CT). All shRNA sequences were cloned into the pSUPER vector (Oligoengine), and the empty pSUPER vector was used as a control. Rat isoform-specific shRNA-targeting sequences (noted as sequence B in text) were previously published (Yoneda et al., 2005) and used in REF52s and rat hippocampal neurons. ROCK isoform-specific shRNA targeting sequences A and C were used for knockdown in CHO.K1s, and sequences A and B were used for rat hippocampal neurons; isoform specificity is characterized in Fig. 1 (A–C) and Fig. S5: ROCK1 shRNA (sequence A), 5′-GGTTAGAACAAGAAGTAAA-3′; ROCK1 shRNA (sequence B), 5′-AATCGGCAGAGGTGCATTTGG-3′; ROCK1 shRNA (sequence C), 5′-GAGATGAGCAAGTCAATTA-3′; ROCK2 shRNA (sequence A), 5′-GCAGAAAGTTCCAAACAGA-3′; ROCK2 shRNA (sequence B), 5′-AACGTGGAAAGCCTGCTGGAT-3′; and ROCK2 shRNA (sequence C), 5′-GTAGAAACCTTCCCAATTC-3′.

Cell culture and transfection

CHO.K1 cells were cultured in low glucose DMEM supplemented with 4 mM L-glutamine and 1 mM sodium pyruvate, 10% FBS, 1% non-

essential amino acids, and 1% penicillin/streptomycin. REF-52 cells were cultured in high glucose DMEM supplemented with 4 mM L-glutamine and 1 mM sodium pyruvate, 10% FBS, 1% nonessential amino acids, and 1% penicillin/streptomycin. For knockdown experiments, cells were transfected with 1 µg shRNA vector and 0.1–0.5 µg of fluorescent-labeled constructs, as noted in the figure legends, with Lipofectamine (Invitrogen). Cells were harvested 48–72 h after transfection. For immunofluorescence assays, cells were plated on 2 µg/ml fibronectin-coated glass coverslips. For live imaging, cells were kept in CCM1.

Neuron culture and transfection

Primary rat hippocampal neuron cultures were prepared as previously described (Goslin and Banker, 1998) and prepared in compliance with the Guide for the Care and Use of Laboratory Animals (National Institutes of Health) as approved by the University of Virginia Animal Care and Use Committee (protocol 2884). In brief, dissociated embryonic day 19 rat hippocampal neurons were cultured on 1 mg/ml poly-L-lysine–coated glass coverslips at a density of ∼70 cells/mm^2 as previously described (Hodges et al., 2011). Primary neurons were cultured in neurobasal medium (Life Technologies) supplemented with B-27 (Life Technologies) and maintained over a rat glial feeder layer. For Fig. 9, neurons were transfected at DIV6 using the published calcium phosphate method (Zhang et al., 2003). For transfection of older neurons (day in vitro [DIV] 17+) in Fig. 4, Fig. 5, and Fig. 6, we used Lipofectamine 2000 (Invitrogen) described previously, to which 100 µM AP-5 was added to the culture media on DIV6 (Hodges et al., 2014). For chemical stimulation of neurons with glycine (Fig. 4), we followed the Park protocol (Park et al., 2004). In brief, DIV19–23 rat hippocampal neurons were preequilibrated in Mg^{2+}-free extracellular solution containing 15 mM NaCl, 0.5 mM KCl, 0.2 mM $CaCl_2$, 3 mM glucose, 1 mM Hepes, 0.5 µM tetrodotoxin, and 1 µM strychnine, pH 7.4, for 30 min followed by 3 min of treatment with 200 µM glycine, and 15 min of washout in Mg^{2+}-free extracellular solution.

Immunocytochemistry

Neurons and fibroblasts were fixed in 4% formaldehyde (ultra-pure EM grade; Polysciences, Inc.) + 4% sucrose for 20 min at room temperature. Alternatively, for staining with phosphospecific antibodies, cells were fixed in 2% formaldehyde + 4% sucrose for 10 min at room temperature followed by incubation in ice-cold methanol for 10 min at −20°C. Cells were permeabilized and blocked in a solution containing 2% BSA, 1% fish skin gelatin, 0.02% saponin, and 15% horse serum in PBS as described previously. The same solution was used for primary and secondary incubations. RLC-PP staining was performed in PBS only. Coverslips were mounted with Vectashield mounting media (Vector Laboratories).

Confocal imaging and analysis

Confocal images were acquired on a laser-scanning microscope (IX81 base; FluoView 1000; Olympus) equipped with a 60×/1.35 NA oil objective (Olympus). Green fluorescent probes (GFP and Alexa Fluor 488) were excited with a 488-nm laser line of a multi-Argon laser, whereas red probes (mCherry, RFP, Alexa Fluor 568, and Rhodamine) were excited with the 543-nm laser line of a He-Ne laser, and the far-red probe Alexa Fluor 647 was excited with the 635-nm line of a diode laser. Fluorescence emission was collected using the following dichroic mirror/filter combinations: SDM560/BA505-525 (GFP), SDM640/BA560-620 (mCherry, RFP, Alexa Fluor 568, and Rhodamine), and BA655-755 (Alexa Fluor 647). Fixed samples were imaged at room temperature, whereas live-cell imaging was performed in HyClone CCM1 media (GE Healthcare) at 37°C. Two-color fluorescence images were collected in a z stack and in sequential mode using FluoView software (Olympus). Image analysis was performed with ImageJ software (National Institutes of Health). Statistical analysis was performed using Sigma Plot 11.0, and unless noted, p-values represent Mann–Whitney rank sum test.

FRAP imaging and analysis

FRAP imaging was performed on an laser-scanning microscope (FluoView 300; Olympus) with a 60×/1.4 NA oil objective, as previously described (Vicente-Manzanares et al., 2008). CHO.K1 cells were imaged in HyClone CCM1 media (GE Healthcare) at 37°C. In brief, MIIB-GFP in the desired region of infection (ROI) was bleached using 100% 488 laser power for 10 consecutive scans, and images were acquired every 10 s for 6 min after bleaching using FluoView software (Olympus). Recovery intensity was normalized to the prebleach intensity.

TIRF microscopy

TIRF images were acquired with an inverted microscope (IX70; Olympus) fitted with a Ludl modular automation controller (Ludl Electronic Products) using a 60×/1.45 NA oil Plan Apochromatic TIRF microscopy objective (Olympus) and charge-coupled device camera (Retiga Exi; QImaging). CHO.K1 cells were imaged in HyClone CCM1 media at 37°C. Images were acquired with MetaMorph Imaging Software (Molecular Devices). GFPs were excited with a 488-nm laser line of a multi-Argon laser, whereas red probes were excited with a 561-nm diode laser.

FRET imaging and analysis

For CFP/YFP FRET acquisition, samples were excited with the 458-nm laser line of a multi-Argon laser, and images were simultaneously acquired using the following dichroic mirror/filter combination: SDM510/BA480-495 (CFP) and BA535-565 (YFP/FRET). Ratiometric FRET images of maximum intensity z projections of the acquired CFP and YFP/FRET images were created using the Biosensor Processing Software 2.1 available from the Danuser laboratory (University of Texas Southwestern, Dallas, TX). Image analysis of the resulting FRET images was performed with ImageJ software.

Traction force measurements

Fluorescent beads (F9910 red [580/605] FluoSpheres; Life Technologies) were embedded at the surface of 5-kPa polyacrylamide gels, prepared as previously described (Engler et al., 2004; Boudou et al., 2009). Polyacrylamide gels were coated with 5 µg/ml fibronectin (F0895; Sigma-Aldrich). CHO.K1 cells were plated overnight on the polyacrylamide gels and released with 0.5% trypsin-EDTA (15400; Life Technologies) to obtain the original bead position. We acquired two images of the fluorescent beads at the surface of the gel, one before trypsinization and one after trypsinization. These two images were aligned to correct for possible x-y drift using the ImageJ plugin Multistackreg (Micheva et al., 2010). The displacement field was then calculated with a particle image velocimetry ImageJ plugin (Tseng et al., 2012). Finally, the traction force field was reconstructed from the displacement field by the Fourier transform traction cytometry method (Butler et al., 2002; Sabass et al., 2008) by using the ImageJ plugin (FTTC [Fourier Transform traction cytometry]; Tseng et al., 2012.

For each cell, we constructed an angular force diagram, in which 0° corresponds to the location of the maximum force ($Force_{MAX}$), by taking the maximum of the force in each direction with a step size of 0.5°. We excluded a disk with a radius of 7 µm at the center of the cell, where we often observed internalized beads. The values of $Force_{Rear}$, $Force_{Front}$, $Force_{Right}$, and $Force_{Left}$ correspond to the mean of the angular force diagram values between −5° and 5°, 175° and 185°, 85° and 95°,

and 265° and 275°, respectively. To correlate traction forces with the Raichu Rac FRET signal, we constructed an angular diagram of the mean FRET within 5 µm of the cell edge with a step size of 3°, in which angle 0° corresponds to $Force_{MAX}$. FRET at $Force_{MAX}$ corresponds to the mean FRET value between −45° and 45°, and FRET at $Force_{180° \text{ from MAX Force}}$ corresponds to the mean FRET value between 135° and 225°.

Online supplemental material

Fig. S1 demonstrates altered microtubule organization in the absence of ROCK1. Fig. S2 supplements Fig. 3 and Fig. 10 by demonstrating that cofilin-S3D specifically rescues polarity of ROCK2, but not ROCK1, knockdown CHO.K1 cells, whereas RLC-T18D, S19D specifically rescues polarity of ROCK1, but not ROCK2, knockdown CHO.K1 cells. Fig. S3 complements Fig. 5 by demonstrating that two other rat ROCK isoform-specific sequences similarly affect synaptic development, resulting in immature filopodia-like spines in ROCK1 knockdown neurons and exaggerated spine head width in ROCK2 knockdown neurons. Fig. S4 demonstrates that ROCK isoforms differentially regulate the distribution of the myosin heavy chain isoforms: ROCK2 regulates NMIIA, whereas ROCK1 regulates NMIIB. Fig. S5 demonstrates that additional ROCK isoform-specific shRNAs similarly affect phosphorylation of cofilin, RLC, MLCP, and LIMK1/2. Video 1 shows that ROCK2 regulates adhesion maturation in protrusions. Video 2 shows that cofilin inactivation rescues adhesion maturation in ROCK2 knockdown cells. Video 3 shows that ROCK1 polarizes adhesion maturation toward the cell rear. Video 4 shows RLC T18, S19 diphosphorylation stabilizes mature adhesions at the rear of the cell. Online supplemental material is available at http://www.jcb.org/cgi/content/full/jcb.201504046/DC1.

Acknowledgments

We would like to thank Samuel Martin-Vilchez for designing the ROCK isoform–specific shRNAs (sequence A) and members of the Horwitz laboratory for reviewing this manuscript.

This work was supported by a National Institute of General Medical Sciences grant (GM23244) to A.R. Horwitz and a Howard Hughes Institute Fellowship administered by the Life Sciences Research Foundation to K.A. Newell-Litwa.

The authors declare no competing financial interests.

Submitted: 9 April 2015
Accepted: 4 June 2015

References

Agnew, B.J., L.S. Minamide, and J.R. Bamburg. 1995. Reactivation of phosphorylated actin depolymerizing factor and identification of the regulatory site. *J. Biol. Chem.* 270:17582–17587. http://dx.doi.org/10.1074/jbc.270.29.17582

Amano, M., M. Ito, K. Kimura, Y. Fukata, K. Chihara, T. Nakano, Y. Matsuura, and K. Kaibuchi. 1996. Phosphorylation and activation of myosin by Rho-associated kinase (Rho-kinase). *J. Biol. Chem.* 271:20246–20249. http://dx.doi.org/10.1074/jbc.271.34.20246

Amano, M., K. Chihara, K. Kimura, Y. Fukata, N. Nakamura, Y. Matsuura, and K. Kaibuchi. 1997. Formation of actin stress fibers and focal adhesions enhanced by Rho-kinase. *Science.* 275:1308–1311. http://dx.doi.org/10.1126/science.275.5304.1308

Beningo, K.A., K. Hamao, M. Dembo, Y.-L. Wang, and H. Hosoya. 2006. Traction forces of fibroblasts are regulated by the Rho-dependent kinase but not by the myosin light chain kinase. *Arch. Biochem. Biophys.* 456:224–231. http://dx.doi.org/10.1016/j.abb.2006.09.025

Bosch, M., and Y. Hayashi. 2012. Structural plasticity of dendritic spines. *Curr. Opin. Neurobiol.* 22:383–388. http://dx.doi.org/10.1016/j.conb.2011.09.002

Bosch, M., J. Castro, T. Saneyoshi, H. Matsuno, M. Sur, and Y. Hayashi. 2014. Structural and molecular remodeling of dendritic spine substructures during long-term potentiation. *Neuron.* 82:444–459. http://dx.doi.org/10.1016/j.neuron.2014.03.021

Boudou, T., J. Ohayon, C. Picart, R.I. Pettigrew, and P. Tracqui. 2009. Nonlinear elastic properties of polyacrylamide gels: implications for quantification of cellular forces. *Biorheology.* 46:191–205.

Burnette, D.T., L. Ji, A.W. Schaefer, N.A. Medeiros, G. Danuser, and P. Forscher. 2008. Myosin II activity facilitates microtubule bundling in the neuronal growth cone neck. *Dev. Cell.* 15:163–169. http://dx.doi.org/10.1016/j.devcel.2008.05.016

Butler, J.P., I.M. Tolić-Nørrelykke, B. Fabry, and J.J. Fredberg. 2002. Traction fields, moments, and strain energy that cells exert on their surroundings. *Am. J. Physiol. Cell Physiol.* 282:C595–C605. http://dx.doi.org/10.1152/ajpcell.00270.2001

Calabrese, B., J.-M. Saffin, and S. Halpain. 2014. Activity-dependent dendritic spine shrinkage and growth involve downregulation of cofilin via distinct mechanisms. *PLoS ONE.* 9:e94787. http://dx.doi.org/10.1371/journal.pone.0094787

Chen, L.Y., C.S. Rex, M.S. Casale, C.M. Gall, and G. Lynch. 2007. Changes in synaptic morphology accompany actin signaling during LTP. *J. Neurosci.* 27:5363–5372. http://dx.doi.org/10.1523/JNEUROSCI.0164-07.2007

Choi, C.K., M. Vicente-Manzanares, J. Zareno, L.A. Whitmore, A. Mogilner, and A.R. Horwitz. 2008. Actin and α-actinin orchestrate the assembly and maturation of nascent adhesions in a myosin II motor-independent manner. *Nat. Cell Biol.* 10:1039–1050. http://dx.doi.org/10.1038/ncb1763

Chrzanowska-Wodnicka, M., and K. Burridge. 1996. Rho-stimulated contractility drives the formation of stress fibers and focal adhesions. *J. Cell Biol.* 133:1403–1415. http://dx.doi.org/10.1083/jcb.133.6.1403

DesMarais, V., M. Ghosh, R. Eddy, and J. Condeelis. 2005. Cofilin takes the lead. *J. Cell Sci.* 118:19–26. http://dx.doi.org/10.1242/jcs.01631

Engler, A., L. Bacakova, C. Newman, A. Hategan, M. Griffin, and D. Discher. 2004. Substrate compliance versus ligand density in cell on gel responses. *Biophys. J.* 86:617–628. http://dx.doi.org/10.1016/S0006-3495(04)74140-5

Even-Ram, S., A.D. Doyle, M.A. Conti, K. Matsumoto, R.S. Adelstein, and K.M. Yamada. 2007. Myosin IIA regulates cell motility and actomyosin-microtubule crosstalk. *Nat. Cell Biol.* 9:299–309. http://dx.doi.org/10.1038/ncb1540

Fortin, D.A., M.A. Davare, T. Srivastava, J.D. Brady, S. Nygaard, V.A. Derkach, and T.R. Soderling. 2010. Long-term potentiation-dependent spine enlargement requires synaptic Ca2+-permeable AMPA receptors recruited by CaM-kinase I. *J. Neurosci.* 30:11565–11575. http://dx.doi.org/10.1523/JNEUROSCI.1746-10.2010

Fukushima, N., and Y. Morita. 2006. Actomyosin-dependent microtubule rearrangement in lysophosphatidic acid-induced neurite remodeling of young cortical neurons. *Brain Res.* 1094:65–75. http://dx.doi.org/10.1016/j.brainres.2006.04.007

Glaven, J.A., I. Whitehead, S. Bagrodia, R. Kay, and R.A. Cerione. 1999. The Dbl-related protein, Lfc, localizes to microtubules and mediates the activation of Rac signaling pathways in cells. *J. Biol. Chem.* 274:2279–2285. http://dx.doi.org/10.1074/jbc.274.4.2279

Goslin, K., and G. Banker. 1998. Rat hippocampal neurons in low-density culture. *In* Culturing Nerve Cells. G. Banker, editor. MIT Press, Cambridge, MA. 339–370.

Heasman, S.J., and A.J. Ridley. 2008. Mammalian Rho GTPases: new insights into their functions from in vivo studies. *Nat. Rev. Mol. Cell Biol.* 9:690–701. http://dx.doi.org/10.1038/nrm2476

Hirose, M., T. Ishizaki, N. Watanabe, M. Uehata, O. Kranenburg, W.H. Moolenaar, F. Matsumura, M. Maekawa, H. Bito, and S. Narumiya. 1998. Molecular dissection of the Rho-associated protein kinase (p160ROCK)-regulated neurite remodeling in neuroblastoma N1E-115 cells. *J. Cell Biol.* 141:1625–1636. http://dx.doi.org/10.1083/jcb.141.7.1625

Hodges, J.L., K. Newell-Litwa, H. Asmussen, M. Vicente-Manzanares, and A.R. Horwitz. 2011. Myosin IIb activity and phosphorylation status determines dendritic spine and post-synaptic density morphology. *PLoS ONE.* 6:e24149. http://dx.doi.org/10.1371/journal.pone.0024149

Hodges, J.L., S.M. Vilchez, H. Asmussen, L.A. Whitmore, and A.R. Horwitz. 2014. α-Actinin-2 mediates spine morphology and assembly of the post-synaptic density in hippocampal neurons. *PLoS ONE.* 9:e101770. http://dx.doi.org/10.1371/journal.pone.0101770

Ishizaki, T., M. Uehata, I. Tamechika, J. Keel, K. Nonomura, M. Maekawa, and S. Narumiya. 2000. Pharmacological properties of Y-27632, a specific inhibitor of rho-associated kinases. *Mol. Pharmacol.* 57:976–983.

Itoh, R.E., K. Kurokawa, Y. Ohba, H. Yoshizaki, N. Mochizuki, and M. Matsuda. 2002. Activation of rac and cdc42 video imaged by fluorescent resonance energy transfer-based single-molecule probes in the membrane of living cells. *Mol. Cell. Biol.* 22:6582–6591. http://dx.doi.org/10.1128/MCB.22.18.6582-6591.2002

Jaworski, J., L.C. Kapitein, S.M. Gouveia, B.R. Dortland, P.S. Wulf, I. Grigoriev, P. Camera, S.A. Spangler, P. Di Stefano, J. Demmers, et al. 2009. Dynamic microtubules regulate dendritic spine morphology and synaptic plasticity. *Neuron.* 61:85–100. http://dx.doi.org/10.1016/j.neuron.2008.11.013

Julian, L., and M.F. Olson. 2014. Rho-associated coiled-coil containing kinases (ROCK): structure, regulation, and functions. *Small GTPases.* 5:e29846. http://dx.doi.org/10.4161/sgtp.29846

Katoh, K., Y. Kano, M. Amano, H. Onishi, K. Kaibuchi, and K. Fujiwara. 2001. Rho-kinase—mediated contraction of isolated stress fibers. *J. Cell Biol.* 153:569–584. http://dx.doi.org/10.1083/jcb.153.3.569

Katsumi, A., J. Milanini, W.B. Kiosses, M.A. del Pozo, R. Kaunas, S. Chien, K.M. Hahn, and M.A. Schwartz. 2002. Effects of cell tension on the small GTPase Rac. *J. Cell Biol.* 158:153–164. http://dx.doi.org/10.1083/jcb.200201105

Kawabata, S., J. Usukura, N. Morone, M. Ito, A. Iwamatsu, K. Kaibuchi, and M. Amano. 2004. Interaction of Rho-kinase with myosin II at stress fibres. *Genes Cells.* 9:653–660. http://dx.doi.org/10.1111/j.1356-9597.2004.00749.x

Kimura, K., M. Ito, M. Amano, K. Chihara, Y. Fukata, M. Nakafuku, B. Yamamori, J. Feng, T. Nakano, K. Okawa, et al. 1996. Regulation of myosin phosphatase by Rho and Rho-associated kinase (Rho-kinase). *Science.* 273:245–248. http://dx.doi.org/10.1126/science.273.5272.245

Kolega, J. 2003. Asymmetric distribution of myosin IIB in migrating endothelial cells is regulated by a rho-dependent kinase and contributes to tail retraction. *Mol. Biol. Cell.* 14:4745–4757. http://dx.doi.org/10.1091/mbc.E03-04-0205

Krey, J.F., S.P. Paşca, A. Shcheglovitov, M. Yazawa, R. Schwemberger, R. Rasmusson, and R.E. Dolmetsch. 2013. Timothy syndrome is associated with activity-dependent dendritic retraction in rodent and human neurons. *Nat. Neurosci.* 16:201–209. http://dx.doi.org/10.1038/nn.3307

Kuo, J.-C., X. Han, C.-T. Hsiao, J.R. Yates III, and C.M. Waterman. 2011. Analysis of the myosin-II-responsive focal adhesion proteome reveals a role for β-Pix in negative regulation of focal adhesion maturation. *Nat. Cell Biol.* 13:383–393. http://dx.doi.org/10.1038/ncb2216

Laukaitis, C.M., D.J. Webb, K. Donais, and A.F. Horwitz. 2001. Differential dynamics of α5 integrin, paxillin, and α-actinin during formation and disassembly of adhesions in migrating cells. *J. Cell Biol.* 153:1427–1440. http://dx.doi.org/10.1083/jcb.153.7.1427

Leeuwen, F.N., H.E. Kain, R.A. Kammen, F. Michiels, O.W. Kranenburg, and J.G. Collard. 1997. The guanine nucleotide exchange factor Tiam1 affects neuronal morphology; opposing roles for the small GTPases Rac and Rho. *J. Cell Biol.* 139:797–807. http://dx.doi.org/10.1083/jcb.139.3.797

Leung, T., E. Manser, L. Tan, and L. Lim. 1995. A novel serine/threonine kinase binding the Ras-related RhoA GTPase which translocates the kinase to peripheral membranes. *J. Biol. Chem.* 270:29051–29054. http://dx.doi.org/10.1074/jbc.270.49.29051

Leung, T., X.Q. Chen, E. Manser, and L. Lim. 1996. The p160 RhoA-binding kinase ROK alpha is a member of a kinase family and is involved in the reorganization of the cytoskeleton. *Mol. Cell. Biol.* 16:5313–5327.

Lynch, G., C.S. Rex, and C.M. Gall. 2007. LTP consolidation: substrates, explanatory power, and functional significance. *Neuropharmacology.* 52:12–23. http://dx.doi.org/10.1016/j.neuropharm.2006.07.027

Machacek, M., L. Hodgson, C. Welch, H. Elliott, O. Pertz, P. Nalbant, A. Abell, G.L. Johnson, K.M. Hahn, and G. Danuser. 2009. Coordination of Rho GTPase activities during cell protrusion. *Nature.* 461:99–103. http://dx.doi.org/10.1038/nature08242

Maekawa, M., T. Ishizaki, S. Boku, N. Watanabe, A. Fujita, A. Iwamatsu, T. Obinata, K. Ohashi, K. Mizuno, and S. Narumiya. 1999. Signaling from Rho to the actin cytoskeleton through protein kinases ROCK and LIM-kinase. *Science.* 285:895–898. http://dx.doi.org/10.1126/science.285.5429.895

Mammoto, A., T. Mammoto, and D.E. Ingber. 2012. Mechanosensitive mechanisms in transcriptional regulation. *J. Cell Sci.* 125:3061–3073. http://dx.doi.org/10.1242/jcs.093005

Matsui, T., M. Amano, T. Yamamoto, K. Chihara, M. Nakafuku, M. Ito, T. Nakano, K. Okawa, A. Iwamatsu, and K. Kaibuchi. 1996. Rho-associated kinase, a novel serine/threonine kinase, as a putative target for small GTP binding protein Rho. *EMBO J.* 15:2208–2216.

Matus, A., M. Ackermann, G. Pehling, H.R. Byers, and K. Fujiwara. 1982. High actin concentrations in brain dendritic spines and postsynaptic densities. *Proc. Natl. Acad. Sci. USA.* 79:7590–7594. http://dx.doi.org/10.1073/pnas.79.23.7590

Merriam, E.B., D.C. Lumbard, C. Viesselmann, J. Ballweg, M. Stevenson, L. Pietila, X. Hu, and E.W. Dent. 2011. Dynamic microtubules promote synaptic NMDA receptor-dependent spine enlargement. *PLoS ONE.* 6:e27688. http://dx.doi.org/10.1371/journal.pone.0027688

Micheva, K.D., N. O'Rourke, B. Busse, and S.J. Smith. 2010. Array tomography: semiautomated image alignment. *Cold Spring Harb Protoc.* 2010:t5527.

Morales, M., and E. Fifková. 1989. In situ localization of myosin and actin in dendritic spines with the immunogold technique. *J. Comp. Neurol.* 279:666–674. http://dx.doi.org/10.1002/cne.902790412

Moriyama, K., K. Iida, and I. Yahara. 1996. Phosphorylation of Ser-3 of cofilin regulates its essential function on actin. *Genes Cells.* 1:73–86. http://dx.doi.org/10.1046/j.1365-2443.1996.05005.x

Nakagawa, O., K. Fujisawa, T. Ishizaki, Y. Saito, K. Nakao, and S. Narumiya. 1996. ROCK-I and ROCK-II, two isoforms of Rho-associated coiled-coil forming protein serine/threonine kinase in mice. *FEBS Lett.* 392:189–193. http://dx.doi.org/10.1016/0014-5793(96)00811-3

Niault, T., I. Sobczak, K. Meissl, G. Weitsman, D. Piazzolla, G. Maurer, F. Kern, K. Ehrenreiter, M. Hamerl, I. Moarefi, et al. 2009. From autoinhibition to inhibition in trans: the Raf-1 regulatory domain inhibits Rok-α kinase activity. *J. Cell Biol.* 187:335–342. http://dx.doi.org/10.1083/jcb.200906178

Nimnual, A.S., L.J. Taylor, and D. Bar-Sagi. 2003. Redox-dependent downregulation of Rho by Rac. *Nat. Cell Biol.* 5:236–241. http://dx.doi.org/10.1038/ncb938

Niwa, H., K. Yamamura, and J. Miyazaki. 1991. Efficient selection for high-expression transfectants with a novel eukaryotic vector. *Gene.* 108:193–199. http://dx.doi.org/10.1016/0378-1119(91)90434-D

Nobes, C.D., and A. Hall. 1999. Rho GTPases control polarity, protrusion, and adhesion during cell movement. *J. Cell Biol.* 144:1235–1244. http://dx.doi.org/10.1083/jcb.144.6.1235

Park, M., E.C. Penick, J.G. Edwards, J.A. Kauer, and M.D. Ehlers. 2004. Recycling endosomes supply AMPA receptors for LTP. *Science.* 305:1972–1975. http://dx.doi.org/10.1126/science.1102026

Parsons, J.T., A.R. Horwitz, and M.A. Schwartz. 2010. Cell adhesion: integrating cytoskeletal dynamics and cellular tension. *Nat. Rev. Mol. Cell Biol.* 11:633–643. http://dx.doi.org/10.1038/nrm2957

Penzes, P., M.E. Cahill, K.A. Jones, J.-E. VanLeeuwen, and K.M. Woolfrey. 2011. Dendritic spine pathology in neuropsychiatric disorders. *Nat. Neurosci.* 14:285–293. http://dx.doi.org/10.1038/nn.2741

Pinto, D., A.T. Pagnamenta, L. Klei, R. Anney, D. Merico, R. Regan, J. Conroy, T.R. Magalhaes, C. Correia, B.S. Abrahams, et al. 2010. Functional impact of global rare copy number variation in autism spectrum disorders. *Nature.* 466:368–372. http://dx.doi.org/10.1038/nature09146

Pontrello, C.G., M.-Y. Sun, A. Lin, T.A. Fiacco, K.A. DeFea, and I.M. Ethell. 2012. Cofilin under control of β-arrestin-2 in NMDA-dependent dendritic spine plasticity, long-term depression (LTD), and learning. *Proc. Natl. Acad. Sci. USA.* 109:E442–E451. http://dx.doi.org/10.1073/pnas.1118803109

Rex, C.S., L.Y. Chen, A. Sharma, J. Liu, A.H. Babayan, C.M. Gall, and G. Lynch. 2009. Different Rho GTPase–dependent signaling pathways initiate sequential steps in the consolidation of long-term potentiation. *J. Cell Biol.* 186:85–97. http://dx.doi.org/10.1083/jcb.200901084

Ridley, A.J., H.F. Paterson, C.L. Johnston, D. Diekmann, and A. Hall. 1992. The small GTP-binding protein rac regulates growth factor-induced membrane ruffling. *Cell.* 70:401–410. http://dx.doi.org/10.1016/0092-8674(92)90164-8

Rösner, H., W. Möller, T. Wassermann, J. Mihatsch, and M. Blum. 2007. Attenuation of actinomyosinII contractile activity in growth cones accelerates filopodia-guided and microtubule-based neurite elongation. *Brain Res.* 1176:1–10. http://dx.doi.org/10.1016/j.brainres.2007.07.081

Ryu, J., L. Liu, T.P. Wong, D.C. Wu, A. Burette, R. Weinberg, Y.T. Wang, and M. Sheng. 2006. A critical role for myosin IIb in dendritic spine morphology and synaptic function. *Neuron.* 49:175–182. http://dx.doi.org/10.1016/j.neuron.2005.12.017

Sabass, B., M.L. Gardel, C.M. Waterman, and U.S. Schwarz. 2008. High resolution traction force microscopy based on experimental and computational advances. *Biophys. J.* 94:207–220. http://dx.doi.org/10.1529/biophysj.107.113670

Sander, E.E., J.P. ten Klooster, S. van Delft, R.A. van der Kammen, and J.G. Collard. 1999. Rac downregulates Rho activity: reciprocal balance between both GTPases determines cellular morphology and migratory behavior. *J. Cell Biol.* 147:1009–1022. http://dx.doi.org/10.1083/jcb.147.5.1009

Sanz-Moreno, V., G. Gadea, J. Ahn, H. Paterson, P. Marra, S. Pinner, E. Sahai, and C.J. Marshall. 2008. Rac activation and inactivation control plasticity of tumor cell movement. *Cell.* 135:510–523. http://dx.doi.org/10.1016/j.cell.2008.09.043

Shaner, N.C., R.E. Campbell, P.A. Steinbach, B.N.G. Giepmans, A.E. Palmer, and R.Y. Tsien. 2004. Improved monomeric red, orange and yellow fluorescent proteins derived from *Discosoma* sp. red fluorescent protein. *Nat. Biotechnol.* 22:1567–1572. http://dx.doi.org/10.1038/nbt1037

Shi, Y., C.G. Pontrello, K.A. DeFea, L.F. Reichardt, and I.M. Ethell. 2009. Focal adhesion kinase acts downstream of EphB receptors to maintain mature dendritic spines by regulating cofilin activity. *J. Neurosci.* 29:8129–8142. http://dx.doi.org/10.1523/JNEUROSCI.4681-08.2009

Shin, K., V.C. Fogg, and B. Margolis. 2006. Tight junctions and cell polarity. *Annu. Rev. Cell Dev. Biol.* 22:207–235. http://dx.doi.org/10.1146/annurev.cellbio.22.010305.104219

Shin, E.-Y., C.-S. Lee, C.-Y. Yun, S.-Y. Won, H.-K. Kim, Y.H. Lee, S.-J. Kwak, and E.-G. Kim. 2014. Non-muscle myosin II regulates neuronal actin dynamics by interacting with guanine nucleotide exchange factors. *PLoS ONE.* 9:e95212. http://dx.doi.org/10.1371/journal.pone.0095212

Stricker, J., Y. Beckham, M.W. Davidson, and M.L. Gardel. 2013. Myosin II-mediated focal adhesion maturation is tension insensitive. *PLoS ONE.* 8:e70652. http://dx.doi.org/10.1371/journal.pone.0070652

Tashiro, A., and R. Yuste. 2004. Regulation of dendritic spine motility and stability by Rac1 and Rho kinase: evidence for two forms of spine motility. *Mol. Cell. Neurosci.* 26:429–440. http://dx.doi.org/10.1016/j.mcn.2004.04.001

Tashiro, A., A. Minden, and R. Yuste. 2000. Regulation of dendritic spine morphology by the rho family of small GTPases: antagonistic roles of Rac and Rho. *Cereb. Cortex.* 10:927–938. http://dx.doi.org/10.1093/cercor/10.10.927

Totsukawa, G., Y. Yamakita, S. Yamashiro, D.J. Hartshorne, Y. Sasaki, and F. Matsumura. 2000. Distinct roles of ROCK (Rho-kinase) and MLCK in spatial regulation of MLC phosphorylation for assembly of stress fibers and focal adhesions in 3T3 fibroblasts. *J. Cell Biol.* 150:797–806. http://dx.doi.org/10.1083/jcb.150.4.797

Tseng, Q., E. Duchemin-Pelletier, A. Deshiere, M. Balland, H. Guillou, O. Filhol, and M. Théry. 2012. Spatial organization of the extracellular matrix regulates cell-cell junction positioning. *Proc. Natl. Acad. Sci. USA.* 109:1506–1511. http://dx.doi.org/10.1073/pnas.1106377109

Tsuji, T., T. Ishizaki, M. Okamoto, C. Higashida, K. Kimura, T. Furuyashiki, Y. Arakawa, R.B. Birge, T. Nakamoto, H. Hirai, and S. Narumiya. 2002. ROCK and mDia1 antagonize in Rho-dependent Rac activation in Swiss 3T3 fibroblasts. *J. Cell Biol.* 157:819–830. http://dx.doi.org/10.1083/jcb.200112107

Uehata, M., T. Ishizaki, H. Satoh, T. Ono, T. Kawahara, T. Morishita, H. Tamakawa, K. Yamagami, J. Inui, M. Maekawa, and S. Narumiya. 1997. Calcium sensitization of smooth muscle mediated by a Rho-associated protein kinase in hypertension. *Nature.* 389:990–994. http://dx.doi.org/10.1038/40187

Umemoto, S., A.R. Bengur, and J.R. Sellers. 1989. Effect of multiple phosphorylations of smooth muscle and cytoplasmic myosins on movement in an in vitro motility assay. *J. Biol. Chem.* 264:1431–1436.

van Bokhoven, H. 2011. Genetic and epigenetic networks in intellectual disabilities. *Annu. Rev. Genet.* 45:81–104. http://dx.doi.org/10.1146/annurev-genet-110410-132512

Vega, F.M., G. Fruhwirth, T. Ng, and A.J. Ridley. 2011. RhoA and RhoC have distinct roles in migration and invasion by acting through different targets. *J. Cell Biol.* 193:655–665. http://dx.doi.org/10.1083/jcb.201011038

Vicente-Manzanares, M., and A.R. Horwitz. 2010. Myosin light chain mono- and di-phosphorylation differentially regulate adhesion and polarity in migrating cells. *Biochem. Biophys. Res. Commun.* 402:537–542. http://dx.doi.org/10.1016/j.bbrc.2010.10.071

Vicente-Manzanares, M., J. Zareno, L. Whitmore, C.K. Choi, and A.F. Horwitz. 2007. Regulation of protrusion, adhesion dynamics, and polarity by myosins IIA and IIB in migrating cells. *J. Cell Biol.* 176:573–580. http://dx.doi.org/10.1083/jcb.200612043

Vicente-Manzanares, M., M.A. Koach, L. Whitmore, M.L. Lamers, and A.F. Horwitz. 2008. Segregation and activation of myosin IIB creates a rear in migrating cells. *J. Cell Biol.* 183:543–554. http://dx.doi.org/10.1083/jcb.200806030

Vicente-Manzanares, M., X. Ma, R.S. Adelstein, and A.R. Horwitz. 2009. Non-muscle myosin II takes centre stage in cell adhesion and migration. *Nat. Rev. Mol. Cell Biol.* 10:778–790. http://dx.doi.org/10.1038/nrm2786

Vicente-Manzanares, M., K. Newell-Litwa, A.I. Bachir, L.A. Whitmore, and A.R. Horwitz. 2011. Myosin IIA/IIB restrict adhesive and protrusive signaling to generate front–back polarity in migrating cells. *J. Cell Biol.* 193:381–396. http://dx.doi.org/10.1083/jcb.201012159

Watanabe, K., M. Ueno, D. Kamiya, A. Nishiyama, M. Matsumura, T. Wataya, J.B. Takahashi, S. Nishikawa, S. Nishikawa, K. Muguruma, and Y. Sasai. 2007a. A ROCK inhibitor permits survival of dissociated human embryonic stem cells. *Nat. Biotechnol.* 25:681–686. http://dx.doi.org/10.1038/nbt1310

Watanabe, T., H. Hosoya, and S. Yonemura. 2007b. Regulation of myosin II dynamics by phosphorylation and dephosphorylation of its light chain in epithelial cells. *Mol. Biol. Cell.* 18:605–616. http://dx.doi.org/10.1091/mbc.E06-07-0590

Wei, Q., and R.S. Adelstein. 2000. Conditional expression of a truncated fragment of nonmuscle myosin II-A alters cell shape but not cytokinesis in HeLa cells. *Mol. Biol. Cell.* 11:3617–3627. http://dx.doi.org/10.1091/mbc.11.10.3617

Wildenberg, G.A., M.R. Dohn, R.H. Carnahan, M.A. Davis, N.A. Lobdell, J. Settleman, and A.B. Reynolds. 2006. p120-catenin and p190RhoGAP regulate cell-cell adhesion by coordinating antagonism between Rac and Rho. *Cell.* 127:1027–1039. http://dx.doi.org/10.1016/j.cell.2006.09.046

Wong, W.T., B.E. Faulkner-Jones, J.R. Sanes, and R.O.L. Wong. 2000. Rapid dendritic remodeling in the developing retina: dependence on neurotransmission and reciprocal regulation by Rac and Rho. *J. Neurosci.* 20:5024–5036.

Worthylake, R.A., and K. Burridge. 2003. RhoA and ROCK promote migration by limiting membrane protrusions. *J. Biol. Chem.* 278:13578–13584. http://dx.doi.org/10.1074/jbc.M211584200

Yee, H.F., Jr., A.C. Melton, and B.N. Tran. 2001. RhoA/rho-associated kinase mediates fibroblast contractile force generation. *Biochem. Biophys. Res. Commun.* 280:1340–1345. http://dx.doi.org/10.1006/bbrc.2001.4291

Yoneda, A., H.A.B. Multhaupt, and J.R. Couchman. 2005. The Rho kinases I and II regulate different aspects of myosin II activity. *J. Cell Biol.* 170:443–453. http://dx.doi.org/10.1083/jcb.200412043

Zhang, H., and I.G. Macara. 2006. The polarity protein PAR-3 and TIAM1 cooperate in dendritic spine morphogenesis. *Nat. Cell Biol.* 8:227–237. http://dx.doi.org/10.1038/ncb1368

Zhang, H., D.J. Webb, H. Asmussen, and A.F. Horwitz. 2003. Synapse formation is regulated by the signaling adaptor GIT1. *J. Cell Biol.* 161:131–142. http://dx.doi.org/10.1083/jcb.200211002